NATIONAL AERONAUTICS AND SPACE ADMINISTRATION

Space Programs Summary 37-61, Vol. I

Flight Projects

For the Period November 1 to December 31, 1969

JET PROPULSION LABORATORY
CALIFORNIA INSTITUTE OF TECHNOLOGY
PASADENA, CALIFORNIA

January 31, 1970

NATIONAL AERONAUTICS AND SPACE ADMINISTRATION

Space Programs Summary 37-61, Vol. I

Flight Projects

For the Period November 1 to December 31, 1969

JET PROPULSION LABORATORY
CALIFORNIA INSTITUTE OF TECHNOLOGY
PASADENA, CALIFORNIA

January 31, 1970

SPACE PROGRAMS SUMMARY 37-61, VOL. I

Prepared Under Contract No. NAS 7-100
National Aeronautics and Space Administration

Preface

The Space Programs Summary is a multivolume, bimonthly publication that presents a review of technical information resulting from current engineering and scientific work performed, or managed, by the Jet Propulsion Laboratory for the National Aeronautics and Space Administration. The Space Programs Summary is currently composed of four volumes:

Vol. I. *Flight Projects* (Unclassified)

Vol. II. *The Deep Space Network* (Unclassified)

Vol. III. *Supporting Research and Advanced Development* (Unclassified)

Vol. IV. *Flight Projects and Supporting Research and Advanced Development* (Confidential)

Contents

I. *Mariner* Mars 1969 Project 1

A. Project Description and Status 1

B. Guidance and Control 2

1. Post-Encounter Performance of *Mariner VI* Spacecraft Battery 2

2. *Mariner* Mars 1969 Power Subsystem 4

II. *Mariner* Mars 1971 Project 9

A. Project Description and Status 9

1. Project Description 9

2. Status 11

B. Guidance and Control 11

1. Solar Panel Array 11

2. Scan Calibration Plan 12

3. Logic Initialization for Scan Control Electronics 14

C. Engineering Mechanics 15

1. *Introduction* 15

2. Temperature Control 15

3. System Test Complex Cabling 20

III. *Viking* Project, Orbiter System and Project Support 21

A. Project Description and Status 22

B. Space Sciences 22

1. Gas Chromatograph/Mass Spectrometer 22

C. Guidance and Control 28

1. Orbiter Power Subsystem 28

2. Radiation Effects of the *Viking* Lander Radioisotope Power System on the Orbiter 32

3. Thrust Vector Control Considerations for Three-Engine Propulsion System Option 33

D. Engineering Mechanics 37

1. Insulation Materials for Mars Lander Application 37

Subject Index 39

I. *Mariner* Mars 1969 Project

A. Project Description and Status

The *Mariner* Mars 1969 mission to conduct exploratory investigations of Mars, using two unmanned spacecraft in the flyby mode, was established in late 1965 and carried out in 1969.

Two spacecraft, *Mariners VI* and *VII*, conceptually modeled on the *Mariner IV* design but modified in terms of flexibility, reliability, and scientific payload to meet the 1969 requirements, were launched aboard *Atlas/Centaur* rockets from Cape Kennedy in 1969 in February and March, respectively. Both launches attained a high level of accuracy, maintained by precise thrust maneuvers.

Tracking and communications were accomplished through the facilities of the Deep Space Network, augmented during the launch phase by elements of the Air Force Eastern Test Range and the Manned Space Flight Network. They were operated during the flight phase by a sophisticated Mission Operations System using the Space Flight Operations Facility at JPL.

The programable nature of the spacecraft flight sequences, particularly the Mars encounter phase, provided for changes and updates in the operations by ground commands that changed the stored sequences of events. A number of anomalous events which occurred during flight were handled in this way, ensuring the desired conduct of the Mars encounter.

The exploration of Mars was conducted in two stages by each spacecraft. First, during the two or three days preceding closest approach to the planet, television pictures and other data were obtained and returned, some data in real-time and some via tape recording and reduced-rate playback (the playback rate was 16,200 bits/s). Then, during approximately 30 min around closest approach, wide- and narrow-angle TV pictures, ultraviolet and infrared atmospheric and surface spectra, and infrared radiometer temperature maps were obtained along preprogrammed groups of swaths, and entry and exit occultation data were obtained. Following this phase, the tape-recorded data were played back (much information had been returned in real-time at the 16,200 bit/s rate).

Approximately 200 television pictures and more than 1000 digital video records were obtained. During near encounter, about 1000 ultraviolet spectral pairs and more than 300 useful infrared spectra were acquired, and thermal maps based on thousands of individual surface-temperature measurements were made. In addition, physical information on the atmosphere in four locations was compiled from the occultation data, and various solar-system constants and planetary ephemerides were improved in accuracy or confirmed by the celestial mechanics experiment, which used spacecraft tracking data. The results of these experiments are being published by the various experimenters in the scientific literature.

Although the Mars mission was operationally completed shortly after the encounters (July 31 and August 5), reduction and analysis of the Mars data continued through this reporting period. In addition, the spacecraft and its instruments were used for various observations of the sky in the months after encounter, and a number of engineering tests of the spacecraft were carried out; analysis of spacecraft performance, especially the investigation of the *Mariner VII* anomaly, continued into this period.

The *Mariner* Mars 1969 mission formally ended on Nov. 1, 1969. However, before that time, tracking operations had been undertaken with a view to supporting a new mission for the still-functioning spacecraft. This mission, which will require spacecraft tracking and ranging through 1970, with intensive coverage in April and May, is to support an experimental test of the general theory of relativity when the spacecraft approach alignment with the sun and the tracking signal passes through the intense gravitational field near the sun. This experiment and the extended mission activity for *Mariner* have been approved in principle, and are presently under way.

B. Guidance and Control

1. Post-Encounter Performance of *Mariner VI* Spacecraft Battery

Eleven days after the *Mariner VI* encounter, having completed its primary mission, the spacecraft was used for post-encounter science experiments principally involving viewing of certain parts of the galaxy with the ultraviolet spectrometer (UVS) and the infrared radiometer (IRR). Two days later, more experimentation was performed with the UVS and IRR, in addition to an experiment with the thermal control flux monitor. In order to successfully perform these experiments, the spacecraft was maneuvered off the sun-line to an extent where the solar array power was insufficient to meet spacecraft demands, resulting in periods of total and partial support by the battery.

Table 1 lists the sequence of events involving battery testing and performance during the experiment period. Up to this time, the battery was approximately 11 mo from date of activation, and had experienced six discharge–charge cycles varying in depth of discharge from 4 to 20%. Although the battery was specifically designed to meet the requirements of the mission only through the encounter period, an analysis of its condition prior to the start of the post-encounter experiments indicated that it was capable of supporting the spacecraft maneuvers. The test consisted of a 15-min charge period, followed immediately by a 15-W on-board test load. Battery performance during the test is shown in Fig. 1.

Shortly after the battery test and analysis period on Aug. 11, 1969, the spacecraft was pitched 81.35 deg off the sun-line. The battery was then supporting the spacecraft with 10.6 A, later increasing to 12.4 A when the science instruments were turned on. Battery performance is shown in Fig. 2. Approximately 797 W-h of an estimated 1350-W-h capacity were supplied by the battery before the solar array reacquired the Sun at the end of

Table 1. Battery testing sequence

Date	GMT, h:min	Event	
8-11-69	00:28	Battery charger on	Fig. 1
	00:43	Battery charger off	
	00:48	Battery test load on	
	01:03	Battery test load off	
	01:40	Spacecraft on battery power	Fig. 2
	04:16	Spacecraft off battery power	
	05:14	Battery charger on	Fig. 3
8-12-69	23:10	Science on–battery charger off	
	00:05	Battery charger on	
8-13-69	23:33	Spacecraft on battery power	Fig. 4
	00:13	Spacecraft off battery power	
	00:26	Spacecraft on battery-solar array	
	04:57	Spacecraft on solar array power	
		Battery charger on	Fig. 5
8-29-69	22:30	Battery charger off	

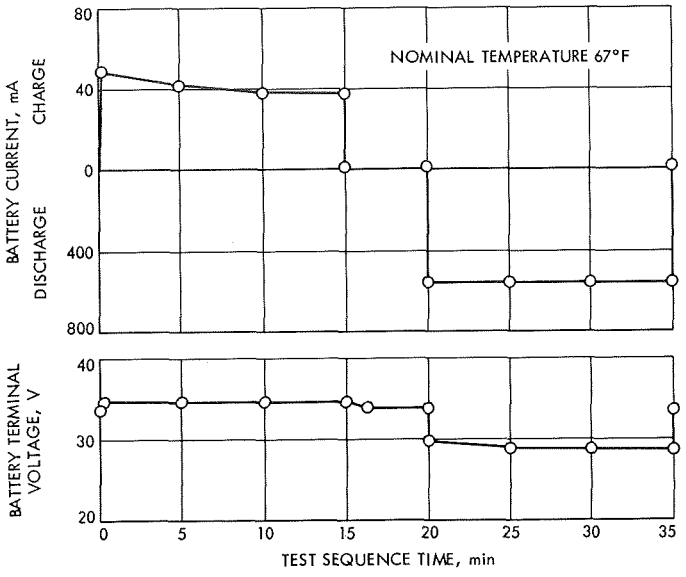

Fig. 1. *Mariner VI* battery current and voltage versus time test sequence

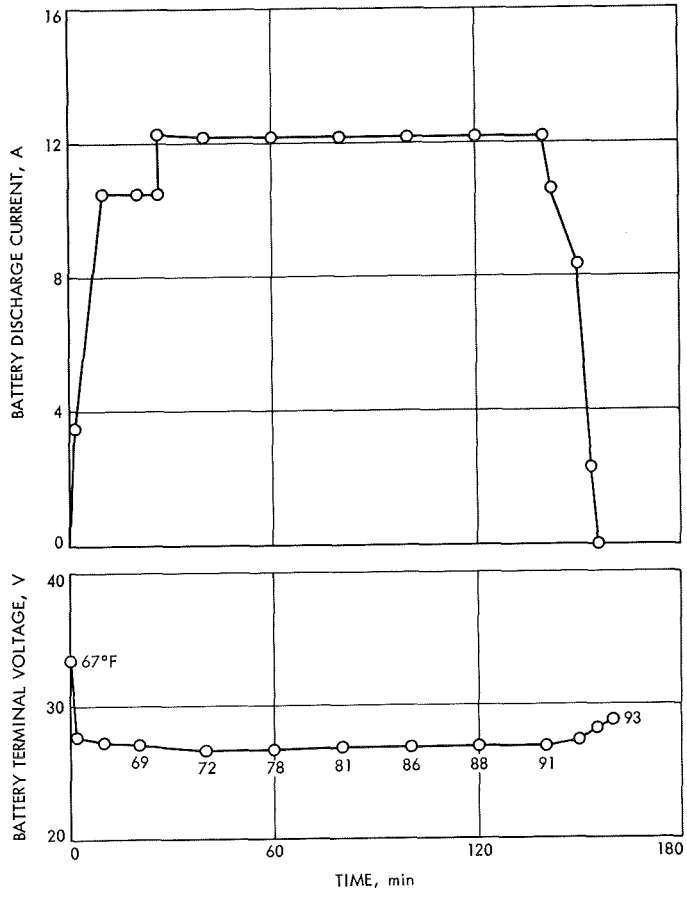

Fig. 2. *Mariner VI* battery current, voltage, and temperature versus time for first post-encounter maneuver

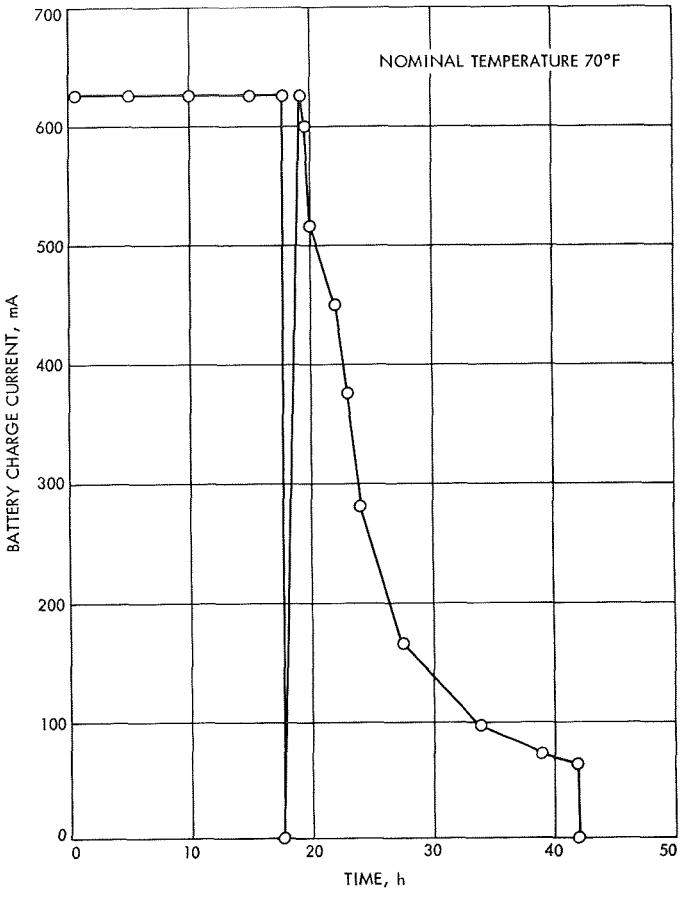

Fig. 3. *Mariner VI* battery charge current versus time after first post-encounter maneuver

the experiment. The battery charger was then turned on to obtain maximum available capacity for the second experiment period two days later. The recharge curve is seen in Fig. 3. One interruption in charging is observed prior to the second experiment period as a result of the science instruments being turned on. A normal function of this command is to also turn off the battery charger. A command was then sent to turn on the charger again.

On August 13 the second experiment period started with a pitch maneuver that resulted in the battery supplying the spacecraft with 11.4 A. At the start of this maneuver, battery capacity was estimated at 970 W-h, the battery charger having returned 417 of the 797 W-h consumed during the first experiment period on August 11. Thirty minutes after the start of this first maneuver on August 13 the spacecraft was pitched back onto the sunline for a short time, then another maneuver was performed that resulted in a battery–solar array share mode for the duration of the experiment. The battery discharge current over the subsequent 4-h period varied from 2.3

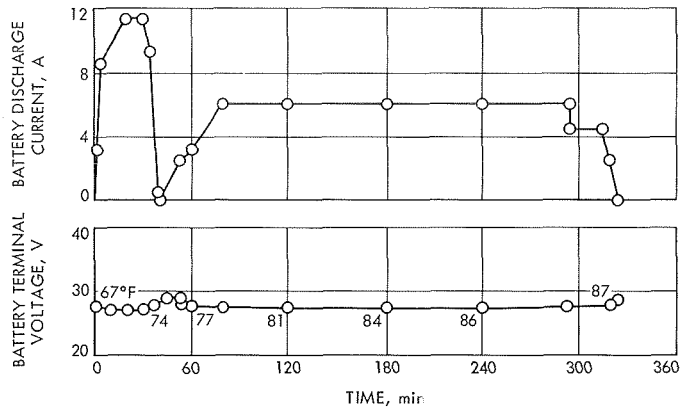

Fig. 4. *Mariner VI* battery current, voltage, and temperature versus time for second post-encounter maneuver

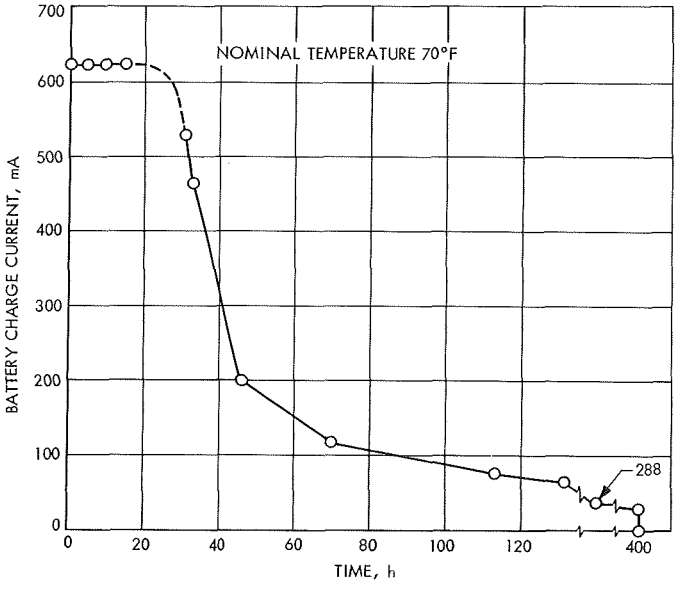

Fig. 5. *Mariner VI* battery charge current versus time after second post-encounter maneuver

to 6.8 A, depending on the spacecraft demand. A total of 877 W-h was supplied during the experiment period on August 13. Figure 4 shows the battery performance parameters during the maneuver. Figure 5 shows the subsequent recharge curve when the battery charger was turned on.

The total time for battery recharge was initially scheduled for 18 days. Due to constraints of available spacecraft tracking time, the battery charger was turned off at 22:30 GMT on August 29, 1969, two days earlier than scheduled. At this time, calculations showed the battery to be 96.2% recharged. Extrapolation of the data indicates that the additional two days would have resulted in a 99.4% charge return. This can be interpreted to mean that the battery was performing, after 6 mo in space, within predictable limits derived from performance data prior to the encounter.

The battery performed extremely well during the experiment periods, with analysis of the data indicating that no apparent degradation had occurred from the time of launch. Voltage and temperature measurements on the battery during charge and discharge periods were within acceptable limits. The performance and data generally indicated that the *Mariner VI* spacecraft battery has a useful lifetime beyond the primary mission requirements, and could continue to have such for some time to come.

2. *Mariner* Mars 1969 Power Subsystem

a. Mariner VII pre-encounter anomaly. The *Mariner VII* power subsystem and other subsystems on the spacecraft, notably the flight telemetry, attitude control and scan subsystems, experienced anomalous events on July 30 and 31, 1969, five days prior to the *Mariner VII* Mars encounter sequence and 7 h prior to *Mariner VI* encounter with the planet. Because of temporary losses of spacecraft communication, detailed circumstances involving much of the anomaly could not be directly monitored, and the multiplicity of spacecraft events prior to and after the anomaly are still under investigation to theorize a best-fit anomaly model. The following serves to describe the sequence of events as they affected the power subsystem, and a more detailed accounting of possible causes for the events will be published when investigations are complete.

Mariner VII pre-encounter battery conditioning. The *Mariner VII* battery conditioning sequence started July 25, 1969 when the 15 W battery test load was commanded on. The *Mariner VII* battery discharged 14.5 h. The total capacity drain was 8.3 A-h, and the discharge sequence was nominal. But the battery recharge cycle that followed was anomalous in several respects.

The battery charger was commanded on July 25, 1969, and after 14 h of charging, the magnitude of the recharge current rate remained significantly higher than typical, as shown in Fig. 6, from point ① onward.

In addition, there occurred a series of unexpected charge current fluctuations during the charge period. It is believed that a small electrical short developed

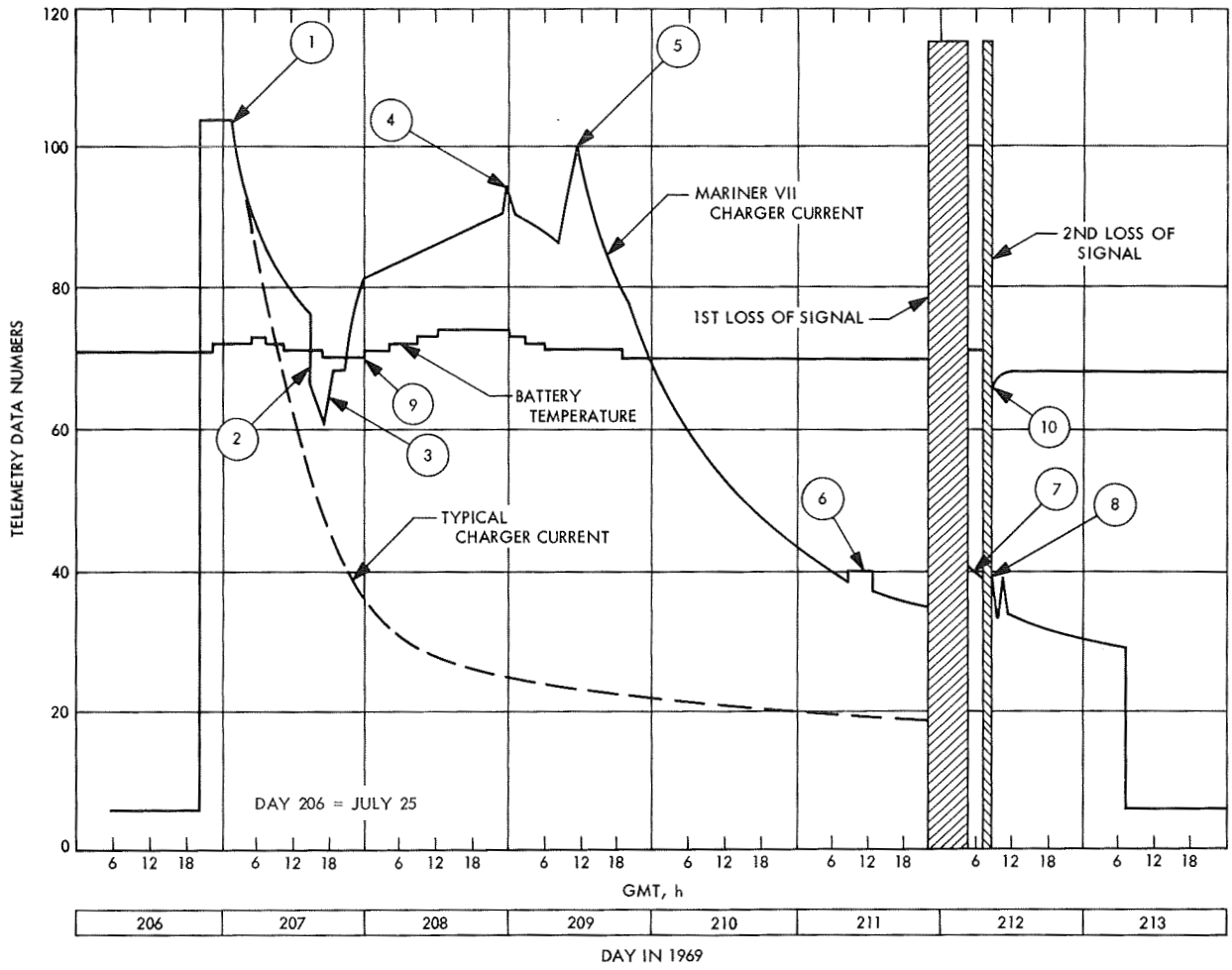

Fig. 6. *Mariner VII* battery charger current and temperature versus time

internal to the battery, which occasionally cleared, caused minor battery voltage changes and charge rate fluctuations shown at points ② to ⑧ in Fig. 6. The battery charger current output is sensitive to battery terminal voltage changes. Battery voltage fluctuations of 100 mV could cause the battery charger output to change from the full charge current rate of 650 mA to a 10-mA trickle charge rate.

The battery temperature profile starting at point ⑨ at 71.4°F unexpectedly rose to peak at 75.5°F, before declining to nominal levels. The unexpected rise in battery temperature could have been caused by a battery internal short.

Five power subsystem telemetry channels were found to be inoperative after the spacecraft engineering telemetry data was reacquired following the first hour loss of signal (Fig. 6). The spacecraft power profile also changed from a near Mars cruise mode to one with gyros on, due to the apparent loss of optical lock on the star Canopus.

Telemetry indicated the battery transducer sensed unexpectedly low temperatures at the end of the second loss of signal at point ⑩ (Fig. 6). The temperature was at 63.9°F before the second signal loss and at 65.2°F when the signal was restored. After 2 h, telemetry again indicated nominal temperature at 69.3°F. The transducer response suggests the possibility that it was cooled by electrolyte evaporation from the battery that may have vented. A small thrust caused by venting could have contributed to spacecraft orbit perturbations at that time.

The power subsystem supported the *Mariner VII* Aug. 5, 1969 Mars encounter sequence in a nominal manner, and on August 12 and 13, 1969, the status of the *Mariner VII* battery was determined by a series of tests. The battery charger was commanded on, and the battery

charge acceptance was unexpectedly low. This was shown by the initial charge rate that was lower than expected, and this declined to lower levels before charger turn-off. The battery test load was then commanded on, and the battery provided lower than expected battery discharge current. The discharge current then dropped to a zero telemetry indication before the test load was turned off.

Circuit verification was made by simultaneously commanding on the battery charger and test load. In this mode, the battery charger is expected to limit at full charge rate, and the battery discharge current telemetry is expected to reach the magnitude a nominal battery would provide. Telemetry indications were as expected, which demonstrated nominal battery charger, test load, telemetry, and circuitry operation. Apparently the *Mariner VII* battery failed in a high internal impedance condition.

b. Extended mission support

Mariner VI array characteristics. Figure 7 describes the projected *Mariner VI* power subsystem support for the extended mission. The sun-oriented curves are projected maximum power points of the array, as the spacecraft heliocentric distance varies with time, and after the following adjustments:

The *Mariner VI* power subsystem unexpectedly entered a battery share mode on October 8, 1969 as the scan motors, science, and IRS motor were turned on at the same time that the gyros and high-power traveling wave tube amplifier (TWTA) were on. The solar array was normal to the sun vector at the time, and the share lasted two data frames, which indicates that the power surge at the *science-on* command was barely adequate to achieve the share mode. The estimated spacecraft peak power surge at the array was 365 W with the *science-on* command. Data points were obtained during this incident and also from the continuous share mode that followed, when the spacecraft was pitched 18 deg from the sun line to enable ultraviolet spectrometer scan of the 1969 B Comet tail. The data placed the *Mariner VI* maximum power point at about 368 W.

The expected maximum power point of the array was 418 W on Oct. 8, 1969 based upon prelaunch data. Accordingly, the array power output appears to have degraded 12% from the Feb. 24, 1969 launch date to Oct. 8, 1969, a daily average of about 0.05%. This average daily array degradation is projected for the balance of the post-encounter mission period, in the absence of firm data at this time to the contrary.

It is estimated that ripple power introduced on the dc power bus by the operation of the booster regulator and the TWTA power converter prevents spacecraft operation within 2% of the array maximum point. The projected solar array P_{max} point determination for the period is, therefore, diminished by this magnitude.

Spacecraft attitude adjustments to maintain spacecraft–earth antenna pointing are time-variant functions of the spacecraft orbit, and changes in pitch, and again in roll, generate a variety of sun shadow patterns that are cast upon the solar panels by the antennas. The shadows reduce array power output.

Array shadowing tests were conducted at JPL with a *Mariner* Mars 1969 spacecraft model in the Celestarium facility. Greater pitch angle magnitudes cause greater power reduction; but roll turn magnitudes for the experiment, which occur after the pitch maneuver, redistribute the shadow pattern to cause much of it to fall between solar panels. The roll maneuver thus recovers some of the array power output lost due to antenna shading after pitch. The greater the pitch angle and resulting shadowing, the greater the power recovery after roll.

Solid curves in Fig. 7, for a spacecraft misoriented from the sun, show the estimated maximum power output of the shaded array as it is pitched off the sun line to start the maneuver that results in maximum shadowing. The dashed curve shows the estimated maximum power output of the shaded array after the roll turn completes the antenna pointing maneuver and reduces array shadowing. A similar set of array curves are provided for optimum pointing pitch angles that are decreased by 8 deg to obtain greater array power and still maintain adequate spacecraft communication with marginal antenna patterns.

Projected Mariner VII array performance. The estimate of the *Mariner VII* sun-oriented maximum power as a function of the orbit is also shown in Fig. 7. Because of the loss of its battery, this spacecraft is largely restricted to sun-oriented operation.

The array curves (Fig. 8) shown for *Mariner VII* are adjusted to match the power output of the *Mariner VI* array, if *Mariner VII* were at the same heliocentric distance on October 8, 1969. This is somewhat conservative, but suits the spacecraft with a failed battery when the

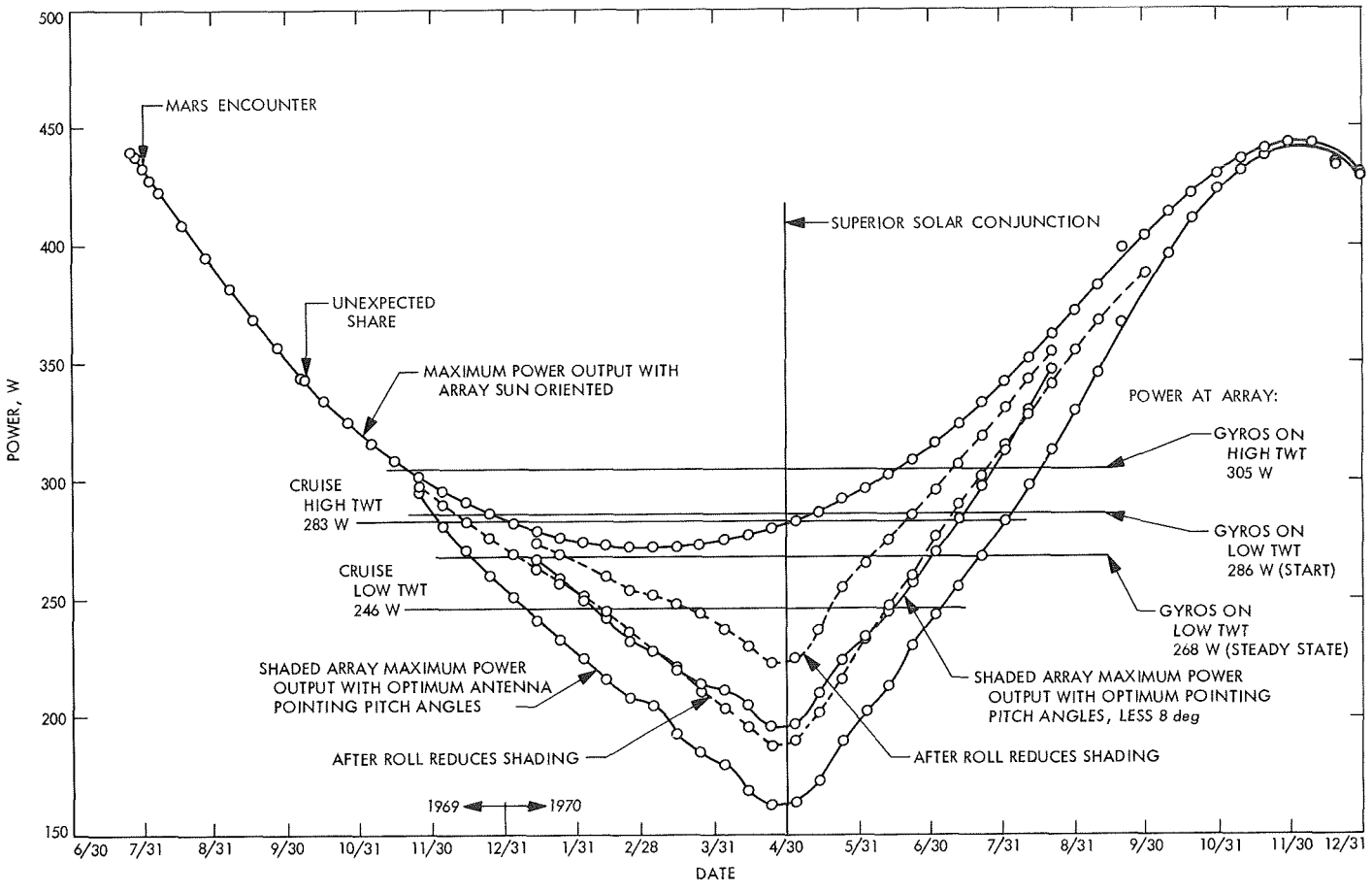

Fig. 7. *Mariner VI* extended mission power subsystem operation with various loads and array orientations

power margin evaluation error is more critical. Other array degradation factors noted for *Mariner VI* apply to *Mariner VII*.

Uncertainty factor. An uncertainty factor reduces the estimated array maximum power of both spacecraft another 5% for possible errors in:

(1) Shadowing investigation for *Mariner VI*.

(2) Estimated heliocentric distance.

(3) Estimated sun intensity.

(4) Estimated average array temperature as it is normal to the sun, and for *Mariner VI* as it is maneuvered from the sun vector, and when shaded.

(5) Graphic representation of the curves.

(6) Telemetry.

Possible array degradation due to proton flare events is not included. Application of 5% uncertainty to *Mariner VII* is another added conservative margin for a spacecraft power subsystem that lacks a battery.

Loads. Average load magnitudes are shown for various *Mariner VI* and *Mariner VII* operating modes in Figs. 7 and 8. Load magnitudes are reflected at the array. Based on the *Mariner VI* data, an array curve can support a given spacecraft load on a given date if it lies above the spacecraft operating mode load line. If the array is shown to support a spacecraft load, the power operating margin for the date is the difference in watts between the load line and the array characteristics.

For example, on June 30, 1970, the *Mariner VI* sun-oriented array will support a gyro turn-on, low-power TWTA by a margin 314 − 286 = 28 W, or 9%. Once the gyro steady-state load is reached, the margin increases to 314 − 268 = 46 W, or 15%.

Intersections of the array characteristics and a load line indicate that the array is unable to support the

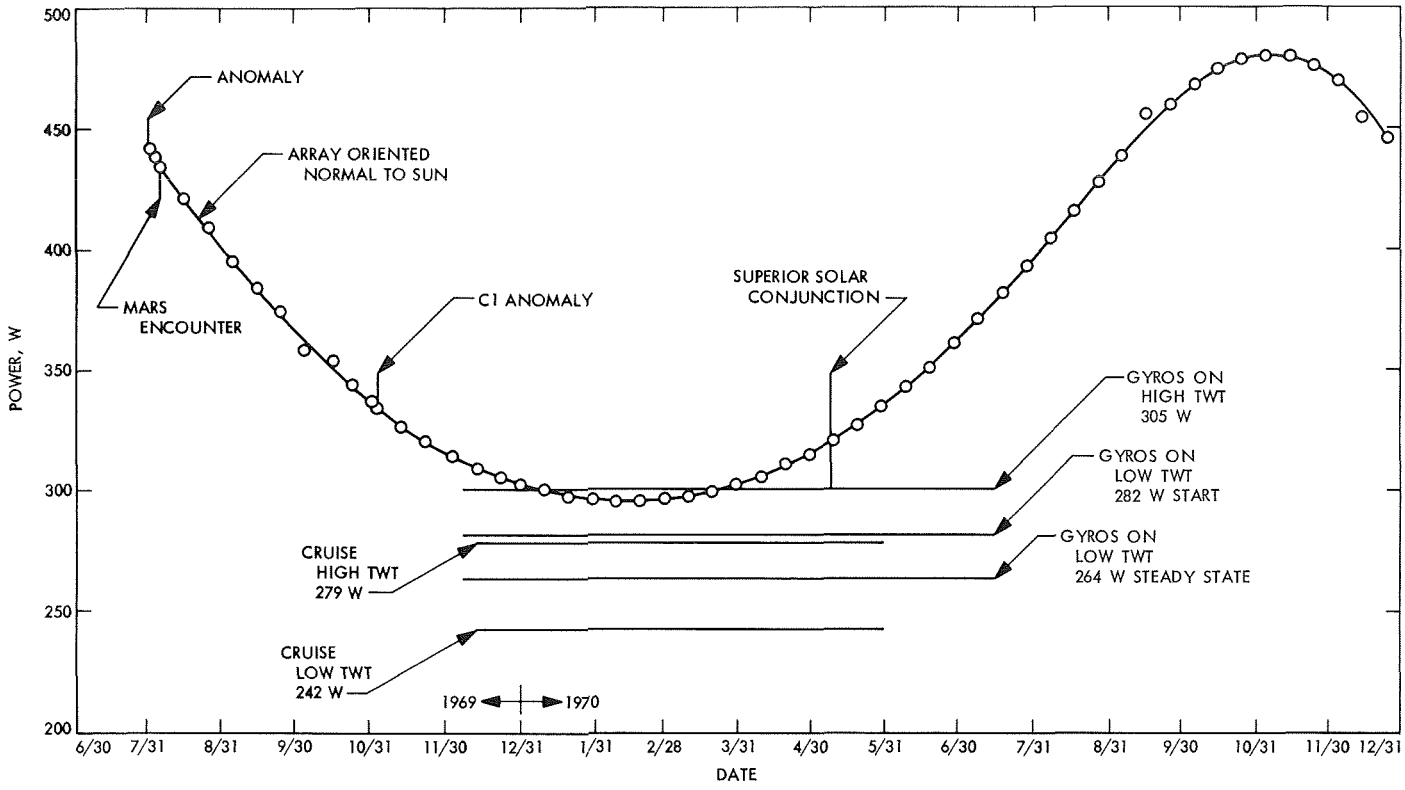

Fig. 8. *Mariner VII* extended mission power subsystem operation versus spacecraft loads

spacecraft load on that date without battery energy contribution; necessitating a share mode.

For example, on July 1, 1970, the *Mariner VI* power subsystem is shown to share with gyros on steady-state, low TWTA, with power margin = 0. The battery discharge rate is 80 W—the estimated minimum battery discharge in the event of share, as noted during the October 8, 1969 incident.

The power subsystem also shares on a given date if the array characteristics lies below a spacecraft load line. For example, on April 30, 1970 the power subsystem of *Mariner VI* shares, with the array oriented for optimum pointing, gyros on, low TWTA. The battery discharge rate is the spacecraft load minus array power plus minimum battery discharge, or 268 − 163 + 80 = 185 W.

There are instances when there occurs a share mode at the start of an operation, and the array recovers full support of the spacecraft load as the operation proceeds. This could be caused either by a surge load that reduces to its lower steady-state magnitude, as when gyros start; or by an array output that increases after roll turns. Two examples are:

First, on April 7, 1970, with a sun-oriented array and low TWTA, it is estimated that *Mariner VI* power will share as gyros are turned on. Battery dissipation = 286 − 275 + 80 = 91 W. Once gyros are in steady state, boosting would probably return power to the array. The margin is 275 − 268 = 7 W.

Second, on June 26, 1970, with the *Mariner VI* array oriented off sun, adjusted 8 deg from optimum pointing, gyros on, low TWTA, the power goes into share after the pitch maneuver. Battery discharges at a rate of 268 − 260 + 80 = 88 W. After the roll turn reduces shading, the array is estimated to once again support the load, with a margin of 289 − 268 = 21 W. The boost converter is inoperative once the array is 5 deg or greater from the sun vector because of the loss of the sun gate signal. But the array is estimated to spontaneously shift the spacecraft load operating point to the more desirable higher potential level when its power conversion capability exceeds in magnitude the spacecraft load, which occurs at the array, by 12 to 16 W.

The *Mariner VII* curves are used in the same manner as *Mariner VI* sun-oriented curves.

II. *Mariner* Mars 1971 Project

A. Project Description and Status

1. Description

The primary objective of the *Mariner* Mars 1971 Project is to place two spacecraft in orbit around Mars that will be used to perform scientific experiments directed toward achieving a better understanding of the physical characteristics of that planet. Principal among these experiments are measurements of atmospheric and surface parameters at various times and locations to determine the dynamic characteristics of the planet. Approximately 70% of the Martian surface will be observed during a minimum of 90 days of orbital operations.

During Mission A, it is planned to map the topography of a large portion of the Martian surface at a resolution significantly higher than that achievable with earth-based methods or by the *Mariner* Mars 1969 spacecraft. In addition, measurements will be made of the composition, density, pressure, and thermal properties of the planet's atmosphere. Other measurements will be directed toward an understanding of Mars' surface temperatures, composition, and thermal properties (particularly at the polar caps); its apparent lack of internal activity; its mass distribution; and its shape.

During Mission B, data will be sought on time-variable features of the Martian surface associated with the wave of darkening wherein both seasonal and secular changes occur. Also, information on atmospheric structure and gross dynamics will be obtained, as well as information directed toward an understanding of Mars' mass distribution, its shape, and its apparent lack of internal activity.

A capability will exist to redirect goals for either mission to the alternate mission if desired. The two launches are anticipated for May 1971, with arrival at the planet during the following November.

An engineering objective of the project is to demonstrate the ability of the spacecraft to perform orbital operations in an adaptive mode wherein information from one orbital pass is used to develop the operations plan for subsequent orbital passes. Studies indicate a high probability that at least one of the spacecraft will survive the sun occultation period which occurs shortly after the 90-day mission is

completed. This makes it possible to conduct an Extended Mission for about a year after orbit insertion. The Extended Mission will probably consist of one or two data taking sequences per week with the capability of recording and playing back about a half-recorder of data (16 TV frames and 11 min of spectrometer data).

One of the *Mariner* Mars 1971 flight spacecraft will be new, and the other will be the spare flight spacecraft of the *Mariner* Mars 1969 Project modified to meet the requirements of the 1971 missions and to enhance mission reliability. The proof test model spacecraft of the *Mariner* Mars 1969 Project will be modified to become the proof test model for the *Mariner* Mars 1971 Project, to be used for preliminary testing and as a simulator in support of flight operations. A major modification for the *Mariner* Mars 1971 mission will be the addition of a rocket motor required to decelerate the spacecraft and place it in orbit around Mars.

Separate scientific instrument subsystems will be required to accomplish the television, infrared radiometer, ultraviolet spectrometer, and infrared spectrometer interferometer experiments given in Table 1. The S-band occultation and celestial mechanics experiments will require no additional equipment on the spacecraft.

Table 1. *Mariner* Mars 1971 scientific experiments and principal investigators

Television	
H. Masursky	Team leader
H. Masursky	PI/U.S. Geological Survey
R. Batson	CI/U.S. Geological Survey
W. Borgeson	
M. Carr	
J. F. McCauley	
D. Milton	
R. Wildey	
D. Wilhelms	
J. Lederberg	PI/Stanford University
E. Levinthal	CI/Stanford University
J. B. Pollack	CI/Cornell University
C. Sagan	CI/Cornell University
G. de Vaucouleurs	PI/University of Texas
W. B. Thompson	PI/Bellcomm
G. A. Briggs	CI/Bellcomm
P. L. Chandeysson	CI/Bellcomm
E. N. Shipley	CI/Bellcomm
B. Smith	PI/New Mexico State University
M. E. Davies	CI/Rand Corp.
W. K. Hartmann	CI/Arizona State University
N. H. Horowitz	CI/Caltech
R. B. Leighton	CI/Caltech
C. B. Leovy	CI/University of Washington
T. B. McCord	CI/MIT
B. C. Murray	CI/Caltech
R. P. Sharp	CI/Caltech

Ultraviolet spectrometer	
C. Barth	PI/University of Colorado
C. W. Hord	CI/University of Colorado
J. B. Pearce	CI/University of Colorado

Infrared interferometer spectrometer	
R. A. Hanel	PI/Goddard Space Flight Center
B. J. Conrath	CI/Goddard Space Flight Center
W. A. Hovis	CI/Goddard Space Flight Center
V. Kunde	CI/Goddard Space Flight Center
G. V. Levin	CI/Biospherics
P. D. Lowman	CI/Goddard Space Flight Center
C. Prabhakara	CI/Goddard Space Flight Center
B. Schlachman	CI/Goddard Space Flight Center

Infrared radiometer	
G. Neugebauer	PI/Caltech
S. C. Chase	CI/Santa Barbara Research Center
E. D. Miner	CI/JPL
G. Munch	CI/Caltech

Celestial mechanics	
J. Lorell	Team leader
J. Lorell	PI/JPL
J. D. Anderson	CI/JPL
W. L. Martin	CI/JPL
W. L. Sjogren	CI/JPL
I. Shapiro	PI/MIT

S-band occultation	
A. Kliore	PI/JPL
D. L. Cain	CI/JPL
G. Fjeldbo	CI/JPL
B. L. Seidel	CI/JPL

PI = Principal investigator, who is the proposer for each experiment.

CI = Co-investigator, who assists the proposer on each experiment.

Team leader heads a particular group of PIs and CIs on an experiment where there is more than one PI.

Management responsibilities for the overall project, the Spacecraft System, the Mission Operations System, and the Tracking and Data System have been assigned to JPL. Lewis Research Center has been assigned management responsibility for the Launch Vehicle System. The launch vehicle will be an *Atlas/Centaur* developed by General Dynamics/Convair.

The *Mariner* Mars 1971 missions will be supported by the Air Force Eastern Test Range launch facilities at Cape Kennedy, the tracking and data acquisition facilities of the Deep Space Network, and other NASA facilities.

2. Status

Interplanetary trajectory and orbit determination studies are in process. A performance analysis report of the launch vehicle indicates a +16-lb performance margin for a 28-day launch period. The orbit insertion and orbit trim design programs are expected to be completed by Feb. 1.

Table 1 gives a complete list of principal investigators for the science experiments; Fig. 1 gives the investigators whose experiments will use television imagery.

Fabrication and testing of the spacecraft prototype equipment is entering the final phase, particularly on selected subsystem hardware, which includes attitude control, propulsion, data automation, data storage subsystem, and television. The engineering test model propulsion assemblies have been delivered, and the dynamic model static tests have begun. Tests of the breadboard TV and its integration with the data automation system and the operation of the ultraviolet spectrometer and IRIS breadboard have been successful. Design freeze dates have now been established for all subsystems.

The mission operations system and tracking data system functional design review was held on October 23 and 24. Near-earth metric data will not be transmitted to the SFOF in real-time; however, orbital parameters computed by the real-time computer system will be.

B. Guidance and Control

1. Solar Panel Array

A program for the fabrication and flight acceptance qualification of *Mariner* Mars 1971 solar panels has been initiated with Electro-Optical Systems, Xerox Corp. Div.,

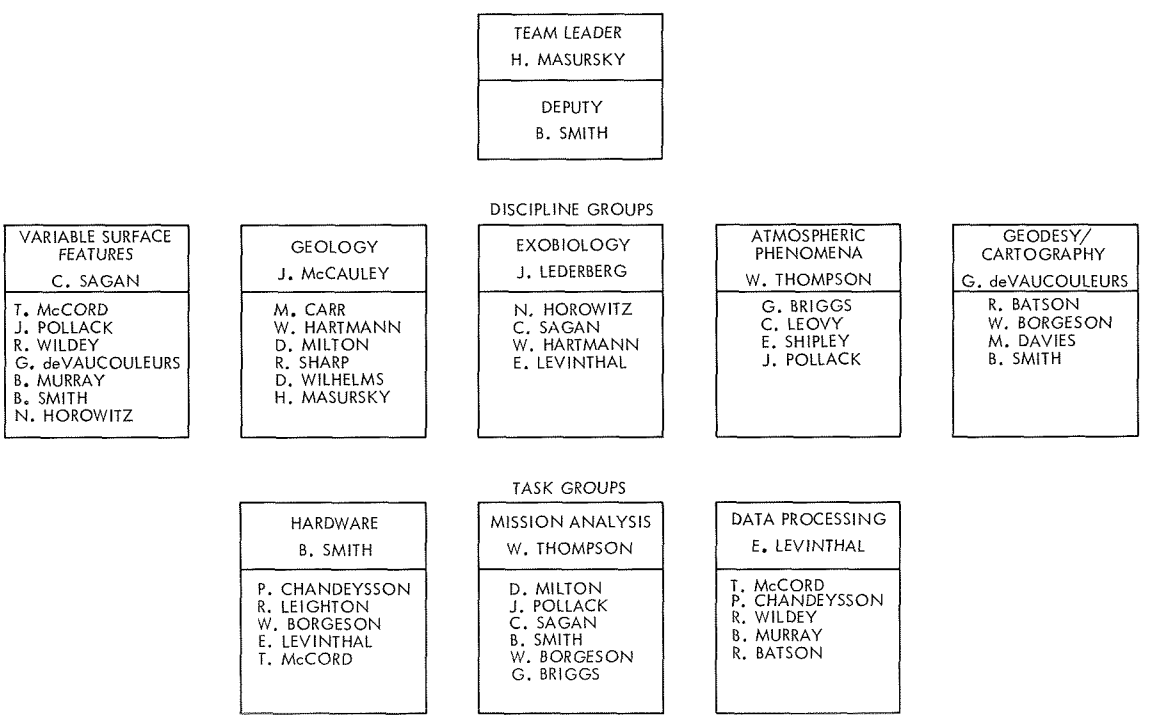

Fig. 1. Television team matrix

under JPL Contract 952483. The program includes manufacturing, electrical measurement of performance and support to JPL in environmental testing.

Seven new panels will be fabricated, and two *Mariner* Mars 1969 residual panels will be refurbished and requalified for the *Mariner* Mars 1971 program. Nine panels will thus be available to support the two missions, four of which will be assigned to a spacecraft and the remaining panel will be available as a spare. The total area of four panels is approximately 83 ft^2 and they will weigh 112 lb. The detailed design description is based on the successful *Mariner* Mars 1969 configuration. Some minor changes will be incorporated in the design, such as the modification to the tip latch of the solar panel structure and changes in fabrication and test procedures to improve production and reduce handling risks.

The solar cells selected for the program to provide the necessary power to the spacecraft are N on P-type, 2 × 2 cm, solder-coated with silver titanium contacts. To each cell a 20-mil-thick fused silica coverglass filter will be attached. The solar cells will be interconnected into submodules by means of tin-plated Kovar ribbons. The submodules are laid out on the panels into six electrically isolated sections.

The electrical performance measurements will be performed at Table Mountain, and the data will be extrapolated to Mars environment conditions. The solar panels will be subjected to flight-acceptance single-panel qualification tests for acoustic and thermal vacuum tests. The type-approval qualification tests were not required, due to the qualified status of the design accomplished during the *Mariner* Mars 69 program.

One temperature transducer will be mounted on the back side of one of the panels to provide information of panel temperatures during flight. To aid in evaluating the power output of the solar panels during the mission, a three-cell transducer will be installed on one of the panels. Output of these cells will be monitored during flight. These outputs are compared to the preflight calibration data and provide relative information on the performance of the panels.

At the present time the fabrication effort is proceeding on schedule. Achievement to date includes the fabrication of approximately 3000 four- and five-cell submodules, representing 40% of the total submodules required for the program. The electrical wiring harnesses for the solar panels are approximately 35% complete.

2. Scan Calibration Plan

a. Introduction. A thorough calibration of the spacecraft electromechanical offsets is required to obtain the desired *Mariner* Mars 1971 scan platform pointing accuracy. A scan calibration plan has been developed to ensure that a thorough calibration will be performed.

The scan calibration plan has two major parts: ground calibration and in-flight calibration. The ground calibration provides baseline information and accuracy. The in-flight calibration refines the ground calibration results to provide the desired accuracy. The ground calibration plan has been developed and is being implemented into system and subsystem test procedures. The in-flight calibration plan is being developed and is contingent on a narrow-angle TV star calibration test.

b. Ground calibration. The basic plan for ground calibration is to calibrate subsystem elements and combine the elements by analysis. Various integrated tests are to be performed to determine interface interactions and to confirm the analysis. The subsystem elements to be calibrated, the subsystems to which they belong, and their electromechanical alignment are illustrated in Fig. 2.

The scan control subsystem has six elements to be calibrated, three for each drive axis. The calibration of potentiometers and associated gear trains will give resistance ratio versus step input or actuator output. The actuator output versus step input is obtained by analysis and checked by an integrated test.

The structure subsystem has five elements to be calibrated. The calibration will give the mechanical offsets within and between the elements as well as at the interfaces with other subsystem elements.

The attitude-control subsystem has one element to be calibrated. The calibration will give the electromechanical offsets of each sensor null from the structure subsystem interface.

The science instrument subsystem has one element to be calibrated. The calibration will give the electromechanical offsets of each science instrument line-of-sight from the structure interface.

The elements will be combined by analysis to obtain the scan platform calibration. The scan platform pointing versus step input and telemetry output will be

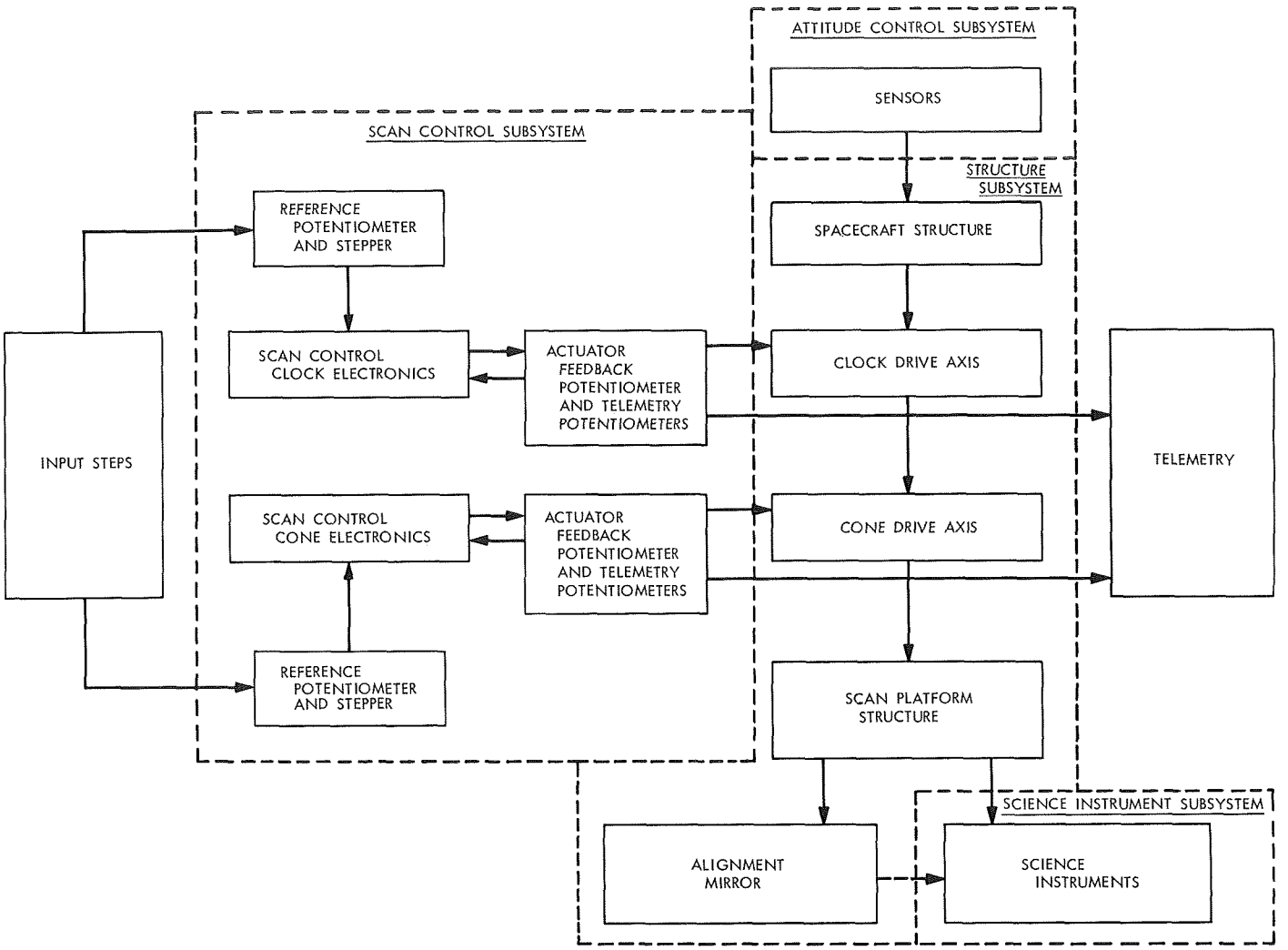

Fig. 2. Scan ground calibration and alignment

obtained by combining all elements except the science instruments. The science instruments offsets from the scan platform will be obtained by combining the mechanical offsets from the scan platform to the science instruments with the electromechanical offsets from the structure interface to the instrument line-of-sight.

A system calibration will be performed on the proof-test model spacecraft to verify the analysis which determines science instruments offsets from the scan platform. The calibration of the scan control subsystem will be checked in the system environment. With the platform in a known mechanical position, the telemetry values will be recorded to establish a system level calibration reference. The accuracy of the ground calibration will be determined by analysis of the measurement accuracy for all the elements calibrated.

c. In-flight calibration. The basic plan for in-flight calibration is to use stars as inertial references to determine the true pointing direction of the narrow-angle TV. The pointing direction of the scan platform and other science instruments will be obtained by analysis, using ground calibration data. The in-flight data for calibration will consist of narrow-angle TV star pictures and telemetry data of the scan platform position and spacecraft limit-cycle position.

The true pointing direction of the narrow-angle TV is obtained by identifying the stars in each TV picture, determining the position of each star in a picture and correcting the spacecraft attitude for limit cycle position. The true pointing direction is compared with the telemetry data of the scan platform position and appropriate corrections to the ground calibration results are made.

The scan calibration accuracy will be greatly improved by the in-flight data, due to the high accuracy of the measurements and the end-to-end nature of the in-flight calibration.

3. Logic Initialization for Scan Control Electronics

a. Introduction. The *Mariner* Mars 1969 scan control system was mechanized so that its clock and cone reference angles were stored as settings on potentiometers. One set of the potentiometers was updatable in flight by pulsing stepper motors. During the *Mariner* Mars 1969 project it was found that the stepper motors stepped inadvertently at power turn-on. Later it was reported that the motors stepped during cruise in response to spacecraft power transients. Since the basic *Mariner* Mars 1969 scan hardware design was used for the *Mariner* Mars 1971 scan control electronics, an investigation was undertaken to determine the cause of the problem and to postulate a solution for the hardware.

b. Circuit description. The cause of the motor misstepping was traced to the motor drive logic circuitry shown in Fig. 3.

The drive circuit consists of four sections; the input noise rejection circuit, the drive logic and drive timing control circuits, and the buffers to energize the motor windings. The stepper motor rotates 360 deg when each of the four buffers is triggered in a predetermined sequence. The timing and width of the motor drive pulses

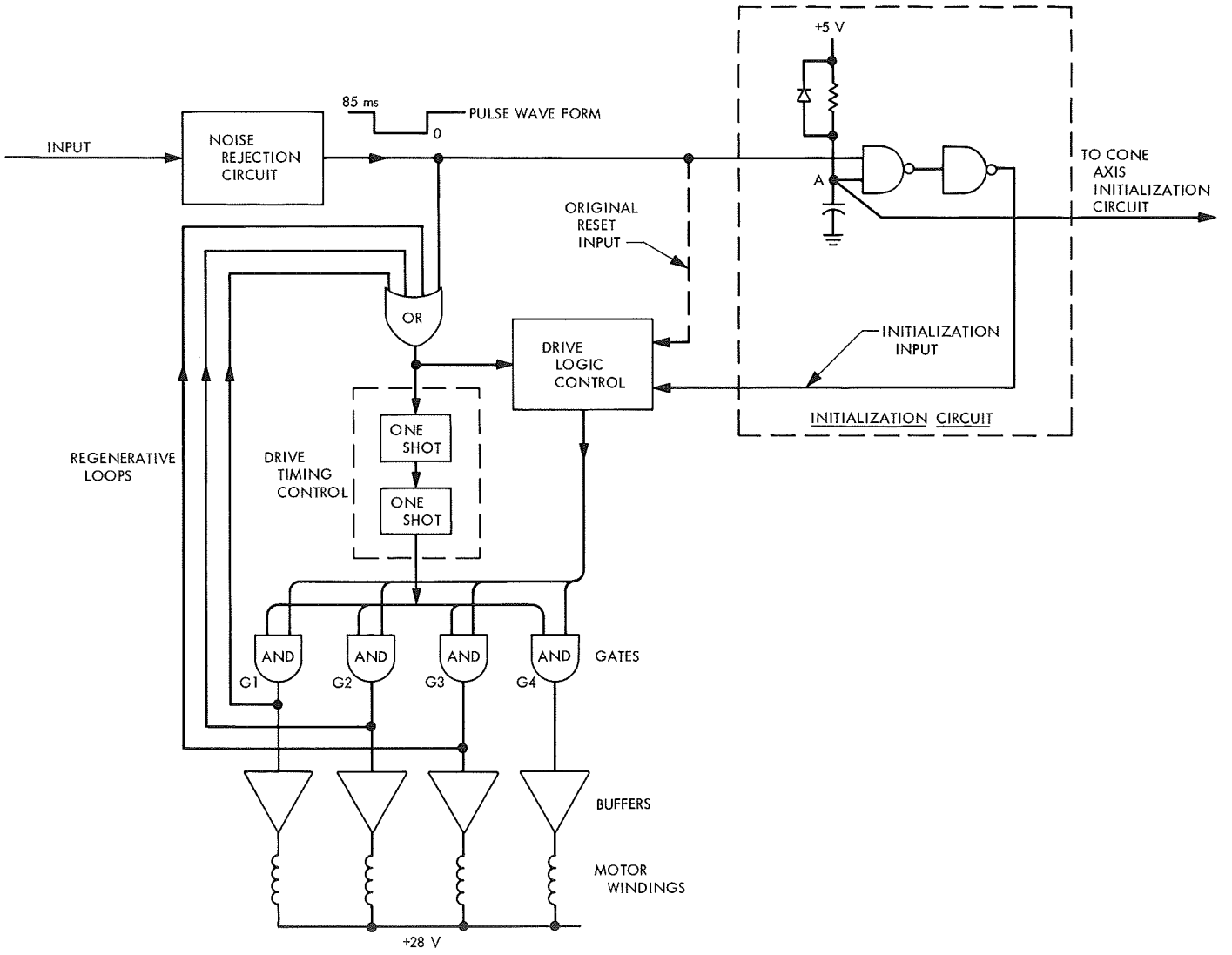

Fig. 3. Scan stepper motor drive circuit (typical of both clock and cone) and initialization circuit

are controlled by two one-shots in the timing control circuit. For each input pulse the circuit regeneratively circulates the pulse through the gates G1, G2, G3, and G4 in a sequence determined by the drive logic. Each pulse results in triggering the corresponding buffer. G4 is the last gate to be triggered in the drive sequence and the regenerative loop is terminated. Thus the motor completes 360 deg of rotation for each input pulse and retains its position after each cycle.

c. Problems and solution. Inadvertent stepping at power turn-on was caused by the one-shots being triggered by the power supply turn on transient. The drive circuit logic is not provided with initialization, since normally this action is provided by the input signal. It was anticipated that a simple logic initialization action to inhibit a regenerative pulse circulation would be sufficient to stop the motor stepping. Further investigation and testing revealed that the drive logic circuit was also affected by the turn-on characteristics of the spacecraft power subsystem. About 35 ms after the initial turn-on, the 50-V 2.4-kHz voltage drops back to about 50% of the steady-state value (Fig. 4). The drive logic elements change their states when the supply voltage is dropped to less than about 50% of the nominal value; thus initiating a regenerative drive cycle. This implies that the logic initialization time required must be longer than 35 ms to be effective. A simple initialization circuit was implemented, as shown in Fig. 3. At power turn-on, the input gate A is held at logical zero for 50 ms. The initialization time constant is determined by the RC combination on the gate input. A diode was placed across the charge resistor to provide a fast discharge of the capacitor in case of power disturbance during normal operation. This improves the capability to reinitialize the drive logic when the power is restored.

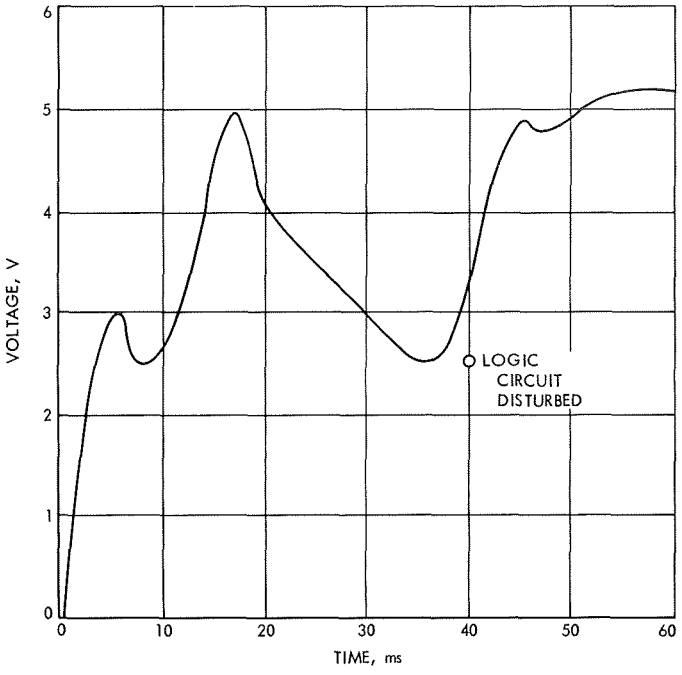

Fig. 4. Response of the +5 Vdc scan power supply to the booster regulator turn-on transient

C. Engineering Mechanics

1. Introduction

Subsystem activities include completion of the detailed design, procurement of most of the flight equipment, and initiation of the spacecraft level structural and thermal tests. This article describes the testing activities in the temperature control area and a brief description of the systems test complex cabling.

2. Temperature Control

a. Rocket engine thermal tests. Temperature control of the propulsion module requires an understanding of the thermal characteristics of the rocket engine assembly during cruise, operation, and post-operation soakback. During temperature control model (TCM) testing the cruise and soakback temperatures will be verified. Test verification of the thermal performance of the engine thermal shields will be done separately.

A series of tests were performed from December 2 through 10, 1969, with the rocket engine assembly. The thermal soakback was simulated through the use of twelve cartridge heaters inserted in a steel thrust chamber with the same external dimensions and thermal mass as the actual beryllium thrust chamber. The thrust chamber was electrically heated to the same average temperature as the beryllium thrust chamber at the end of an actual vacuum firing. The purpose of the test series was:

(1) To verify the operation of the electrically heated steel thrust chamber with actual engine hardware surrounding the thrust chamber.

(2) To experimentally verify the heat capacity of the engine by running two soakback profiles with 300 and 450 W-h of energy being dissipated in the steel thrust chamber during a 900-s simulated firing.

(3) To determine the suitability of using the electrically heated thrust chamber for cruise tests during TCM testing. During TCM testing the spacecraft will be positioned such that it will be time consuming to

exchange the beryllium thrust chamber and the electrically heated steel thrust chamber. Additionally, time will be saved by eliminating a simulator warm-up, backfill, pumpdown, and shroud cooling sequence.

Four tests were performed to compare the cruise temperatures. Tests with the solar flux at approximately earth and Mars intensity were performed on the rocket engine assembly with the beryllium chamber installed and then the electrically heated steel thrust chamber installed. For the cruise tests the cartridge heaters were not energized.

Table 2 shows the comparison of several components of the rocket engine assembly. From these temperatures and the remaining temperatures it was concluded that the steel thrust chamber may be substituted for the beryllium thrust chamber during cruise tests.

Table 3 shows the solar fluxes and total fluxes that were measured following the test of the rocket engine assembly. The primary absolute cavity radiometer (PACRAD) and the temperature control flux monitor (TCFM) were used to measure these fluxes. The overload condition of the TCFM was expected, as it is not designed to measure a flux of this magnitude.

Table 2. Comparison of critical engine temperatures during cruise for two thrust chambers at two solar fluxes

Component	Temperature, °F			
	Earth intensity		Mars intensity	
	Beryllium chamber	Steel soakback chamber	Beryllium chamber	Steel soakback chamber
Thrust chamber	158	158	83	82
Injector	150	144	78	73
Valve seat	140	135	71	66

Table 3. Solar and total intensity measurements

Conditions	Solar	Background
90°F Shroud, 1000 intensity control, no filter	PACRAD 142 mW/cm^2 TCFM overload	49 mW/cm^2
30°F Shroud, 450 intensity control, 63% filter	PACRAD 75 mW/cm^2 TCFM 72.8 mW/cm^2	31 mW/cm^2 31 mW/cm^2

During testing it was found that the electrical heaters could be used to shorten considerably the time necessary to establish thermal steady-state conditions. This will be useful during TCM testing when test conditions are changed from a Mars solar flux to an earth solar flux. The rocket engine assembly can then be electrically heated to approximately the temperature expected at earth intensity, thereby hastening the final steady-state temperatures. Without the use of the heater it would be necessary to wait at least 12 h for steady-state engine temperatures.

Following the cruise tests two soakback tests were performed. In the first 300 W-h were dissipated in 900 s to simulate a nominal soakback condition. In the second test 450 W-h were dissipated also in 900 s to verify operation of the soakback thrust chamber at the higher temperature condition. The temperature–time histories of the injector and valve seat are shown in Figs. 5 and 6. The temperature–time history of an injector and valve seat from an actual test firing (Test DD 405) at Edwards Test Station (ETS) are also shown. In an actual test, the fuel and oxidizer cool the valve seat and injector during engine operation. This accounts for the relatively constant temperature of the valve seat and injector during an actual firing.

b. Upper thermal blanket evaluation tests. A series of tests were recently completed in which the thermal performance of several different upper thermal blanket prototypes were evaluated. The parameter chosen to describe this performance was effective emittance ϵ_{eff} based on the average temperature within the blanketed cavity at the blanket–bus interface (adiabatic plane). This performance data was then combined with other considerations, such as weight, time required for fabrication, ease of fabrication, and venting capability to provide a basis for the selection of a candidate flight blanket. Appropriate seams and cutouts were then made in the candidate blanket and it was retested to determine the effect which the more flightlike configuration might have on thermal performance. This candidate blanket then underwent several rapid decompressions in order to ascertain whether or not it was properly and adequately vented.

In addition to the aforementioned tests on the complete upper thermal blanket, an additional test was performed using only the rocket engine thermal blanket, rocket engine thermal shield, and that 30-in.-diam portion of the upper thermal blanket which lies beneath them. The purpose of the test was to determine the

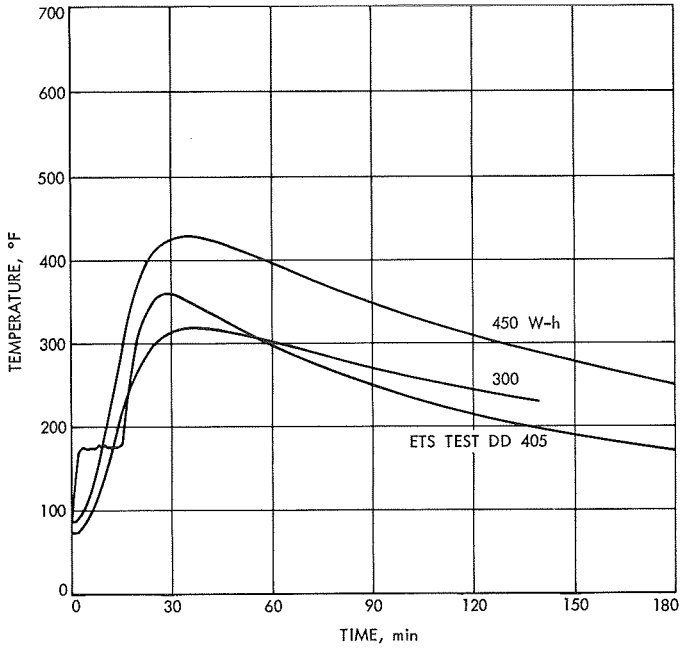

Fig. 5. *Mariner* Mars 1971 rocket engine assembly injector temperature versus time

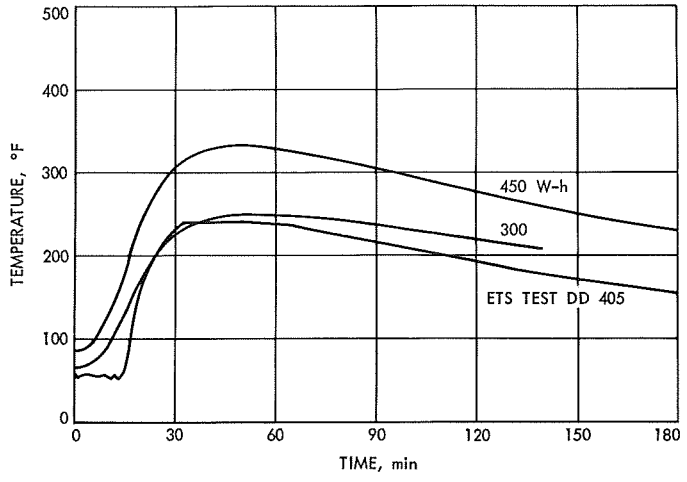

Fig. 6. *Mariner* Mars 1971 rocket engine assembly valve seat temperature versus time

effectiveness of the rocket engine thermal blanket and shield by simulating a rocket engine firing under good vacuum conditions and monitoring temperatures at various locations within the blanket.

Upper thermal blanket effective emittance tests. The test fixture for the emittance tests consisted of an aluminum skeleton structure which provided the proper configuration at all of the points where the upper thermal blanket comes in contact with the propulsion module.

A solid octagonal aluminum plate with the outer dimensions of the upper ring of the octagon structure served as the bus-propulsion module interface. It was to this plate that the skeleton structure was mounted. This baseplate was, in turn, mounted to another plate of equal dimensions. Both the baseplate and the guardplate were equipped with heaters and were insulated from one another by means of fiberglass standoffs and three layers of double-aluminized Mylar. Power was provided to the blanket interior through the baseplate heater and baseplate and guardplate temperatures were matched with the guardplate heaters, thereby providing a nearly adiabatic plane at the bus-propulsion module interface.

The blanket configuration for the first seven modes consisted of different combinations of various blanket components as described in Table 4. In each configuration there were no penetrations through the blanket except where it interfaced with the baseplate. Typically the Armalon layer was tied to the baseplate in a flight-like manner (drawstring/screw-eye arrangement) but the blanket beneath the Armalon, not being seamed, was simply taped to the Armalon around its lower periphery. The first seven modes were selected to investigate the following areas of interest:

(1) The relationship between number of layers and effective emittance (Modes 1, 3, 4 and 6).

(2) The effect of a low-emittance outer layer on effective emittance (Mode 2 versus Mode 1).

(3) Reproducibility of blanket construction (Mode 5 versus Mode 1).

(4) Comparison of *Mariner* Mars 1969 materials and fabrication techniques with those proposed for *Mariner* Mars 1971 (Mode 7 versus Mode 1).

The blanket tested in Mode 3 (Dacron inner layer, fifteen ⅛-mil Mylar/*Mariner* Mars 1971 net layers, and an Armalon outer layer) was selected as the flight candidate blanket for the following reasons:

(1) The 14% decrease in ϵ_{eff} (2.5 W) afforded by the 20-layer blanket over the 15-layer blanket was not considered sufficient to warrant the extra material, weight, and fabrication time required for the additional five layers.

(2) Although the *Mariner* Mars 1969 blanket compares favorably with the *Mariner* Mars 1971 blanket on

Table 4. Upper thermal blanket effective emittance test results

Mode No.	Blanket configuration[a] Inner to outer layer →								Power, W	Average temperature, °F	Effective emittance ε_{eff}	Weight, lb
	D	10	5a	5b	69	A	M	Other				
1	√	√				√			18.15	70.6	0.0064	8.6
2	√	√				√	√		15.15	71.0	0.0054	
3	√	√	√			√			16.1	72.0	0.0056	10.2
4	√	√	√	√		√			13.6	72.6	0.0048	11.8
5	√		√	√		√			18.8	70.5	0.0067	8.7
6	√		√			√			23.1	70.8	0.0083	7.0
7	√				√	√			17.5	71.2	0.0062	9.4
8	√	√	√			√		[b]	18.4	70.9	0.0066	
9	√	√	√			√		[b]	15.3	38.9	0.0069	

[a]Definition of blanket configuration symbols:

D Dacron slipcover. A single-layer blanket made of Dacron cloth to serve as a removable inner layer.

10 Ten-layer blanket. Ten layers of 1/8-mil Mylar, aluminized on both sides, alternated with ten layers of Nylon net (*Mariner* Mars 1971 net) so that the blanket has a Mylar inner layer and a net outer layer.

5a and 5b Five-layer blankets. Each made up of five layers of 1/8-mil Mylar, aluminized on both sides, alternated with five layers of Nylon net (*Mariner* Mars 1971 net) so that each blanket has a Mylar inner layer and a net outer layer.

69 Blanket constructed with *Mariner* Mars 1969 materials and techniques, made up of ten layers of 1/4-mil Mylar, aluminized on both sides, alternated with ten layers of Nylon net (*Mariner* Mars 1969 net) so that the blanket has a Mylar inner layer and a net outer layer.

A Armalon slipcover. A single-layer blanket made of Armalon (Beta cloth) to serve as a removable outer layer.

M Low-emittance Mylar slipcover. A single-layer blanket made of 1/2-mil Mylar, aluminized on both sides, to serve as a removable outer layer.

[b]Flightlike blanket with engine and omni-cutouts covered with 2-mil aluminized Kapton, aluminum side out.

an effective emittance basis, it was eliminated from contention due to its additional weight (10%) and the fact that it is somewhat more difficult to fabricate than a blanket of the *Mariner* Mars 1971 type.

(3) The low-emittance outer layer used in Mode 2 provides a substantial (16%) decrease in effective emittance over the high-emittance (Armalon) outer layer, but unfortunately, the Mylar outer layer used on Mode 2 would severely overheat when subjected to flightlike solar irradiation. Any alternative which would maintain an acceptable temperature must necessarily have a higher emittance, thereby giving up at least part of the advantage of a low-emittance outer layer and undoubtedly presenting a more difficult problem with regard to blanket handling and cleaning. The superior durability of the Armalon outer layer outweighed any advantages in effective emittance which a low-emittance outer layer might provide.

Once the flight candidate blanket was selected, the rocket engine and omni-antenna cutouts were made, and all flightlike seams were incorporated (Fig. 7). A flightlike closure was made at the blanket opening along the outboard side of the omni-antenna (i.e., lacing) instead of the simple taped overlap used for the first seven modes. The engine and omni-holes were then covered with 2-mil aluminized Kapton (aluminum side out), and the blanket was tested at two different temperature levels (Modes 8 and 9). The results indicated that the total seam effect was an increase of 20% in effective emittance (or 2.3 W).

Ballooning tests. After the effective emittance tests had been completed, the aluminized Kapton covers over the engine and omni-holes were removed, and the blanket was subjected to three rapid decompression cycles (Fig. 8).

Although the blanket appeared to be severely strained during the maximum rate pumpdown in particular, it remained intact throughout the ballooning tests, and no damage of any kind was observed at their completion.

The test was considered to be conservative even for the nominal *Atlas/Centaur* pressure profile due to the large

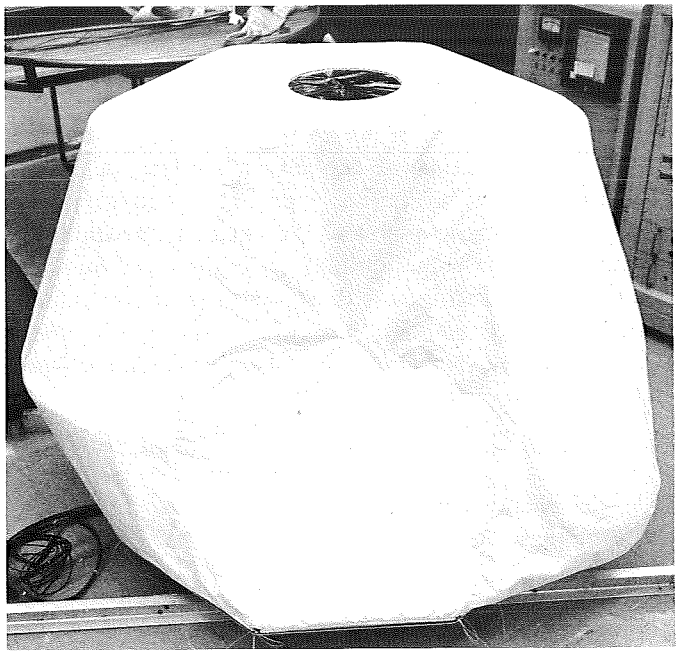

Fig. 7. Flight candidate upper thermal blanket

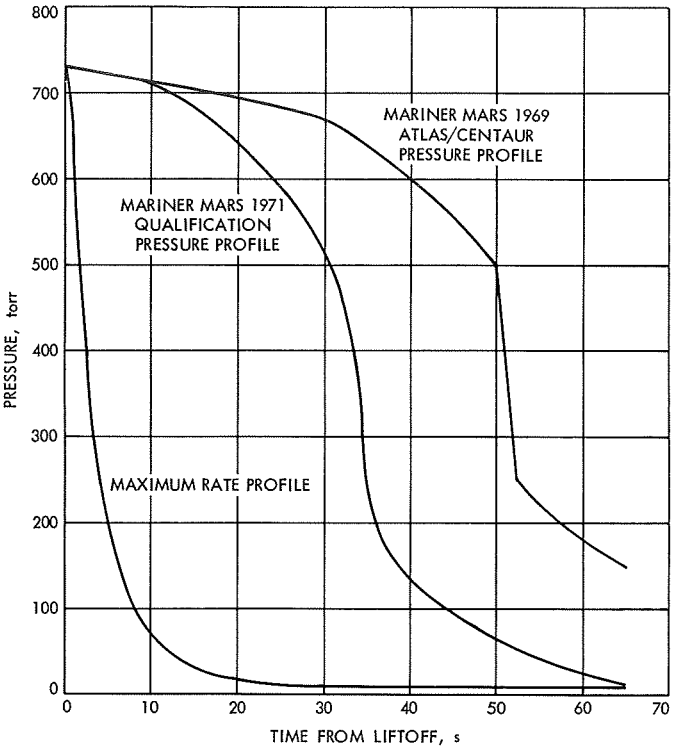

Fig. 8. Upper thermal blanket ballooning test pressure profiles

volume of air within the blanketed cavity which would normally be taken up by propulsion system tankage.

Rocket engine thermal blanket test. Figure 9 shows the test fixture for the simulated engine firing with the experimental rocket engine thermal blanket in place. The blanket made of aluminized Kapton is cut away at various diameters to expose the Armalon outer layer of the upper thermal blanket underneath. Beneath the Armalon are several thermocouples at each of the various diameters to provide the data necessary for optimizing the rocket engine thermal blanket diameter. The mocked-up nozzle extension is made of mild steel and is heated internally by three 6-kW quartz-iodine infrared lamps. The rocket engine thermal shield (gold-plated titanium) is also shown in place and instrumented.

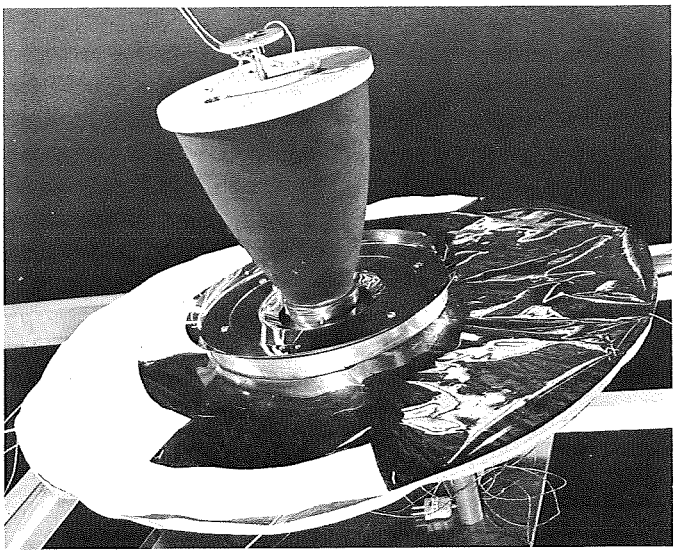

Fig. 9. Test fixture for rocket engine thermal blanket and shield

Although several real test firings have been performed at Edwards Test Station with the same blanket and shield appropriately installed, vacuum conditions during those tests were not considered good enough to prevent gaseous conduction. As a result, the ETS tests appear to be unconservative with respect to blanket and shield temperatures.

This test, on the other hand, is considered conservative due to: (1) a vacuum of 5×10^{-5} torr or better over the entire test duration, (2) nozzle extension temperatures higher than those recorded during actual firings, and (3) a camphor-blacked outer surface on the nozzle extension providing an emittance (and radiant flux) higher than that expected in flight.

The results indicated that, indeed, the gold-plated titanium shield and the outer blanket layer rose to temperatures higher than those at ETS. Also, as expected, the inner blanket layers remained cooler than they did under ETS conditions. A post-test inspection of the portion of upper thermal blanket installed under the rocket engine thermal blanket indicated that internal mylar layers had overheated and bonded themselves together within a 12-in. radius of the nozzle centerline under those areas where the upper thermal blanket was unprotected (i.e., no Kapton rocket engine thermal blanket above it). To prevent this kind of failure the minimum rocket engine thermal blanket diameter would have to be 24 in.

3. System Test Complex Cabling

a. Introduction. The purpose of the system test complex (STC) cables is the routing of the required power and signals to adequately test the spacecraft from the various subsystem support equipment (SE). These cables are categorized into the following types: (1) umbilical, (2) direct access, (3) control (hoods and external stimuli), (4) interconnect (console to console), (5) computer, and (6) coaxial (RF). Also, these categories, particularly the first three, can be divided into two groups which are dependent on the type and location of the testing. The first of these groups is used at the spacecraft assembly facility (SAF) where the spacecraft is assembled and tested at a system level. The second group consists of cables used at the space simulator facility (SSF) where the spacecraft is environmentally tested.

This article is devoted to the changes to the *Mariner* Mars 1969 STC cabling in order that it may satisfy the testing parameters of *Mariner* Mars 1971.

With the exception of the RF subsystem, all other spacecraft subsystems either were new equipment or drastically revamped to fulfill the orbiting capability of the mission. Approximately half of required cabling was affected. New cabling was designed to match the direct access, umbilical or control testing of these subsystems which included pyrotechnics, science, power and attitude control.

Examples of these changes are as follows:

(1) Command. Additional return wires and shielding for noise reduction purposes.

(2) Power. A separate cable series to accommodate the new Ni-cad battery.

(3) Attitude Control. New hoods for the sungate, cruise and acquisition sun sensors necessitated a completely revised cabling network.

(4) Pyrotechnics. Shielding was provided for the added propulsion firing monitor circuits.

(5) Science. New test equipment and instrument (infrared interferometer spectrometer and SE simulators) caused extensive changes to this subsystem's cabling.

III. *Viking* Project, Orbiter System and Project Support

A. Project Description and Status

The primary objective of the *Viking* Project is to send two vehicles to the planet Mars to perform scientific experiments directed toward enhancing current knowledge about the physical characteristics of the planet, particularly its capability for supporting life and possible evidence of life. The two vehicles, each consisting of an orbiter system and a lander system, are anticipated for launch during 1973. The orbiter system will be developed by JPL, and the lander system will be developed by the Martin-Marietta Corp. Langley Research Center has overall management responsibility for the *Viking* Project.

The orbiter system will transport and inject the lander system at the appropriate point for a selected landing site and will relay telemetered data from the lander to earth. Scientific instruments on the orbiter will be used to measure atmospheric and surface parameters at various times and locations to determine the dynamic characteristics of the planet. The topography of Mars will be mapped during orbital operations, with special emphasis on mapping the proposed landing site prior to deorbit of the lander system. Both visual and infrared coverage will be possible during the presently planned 90 days of orbital operations.

During entry and after landing, the scientific instruments on the lander will measure Mars' atmospheric composition, temperature, pressure, and density. After landing, the topography of the landing site will be mapped, and measurements will be made of the planet's surface composition, temperature, pressure, humidity, and wind speed. Of particular interest in the surface measurements are the type of organic compounds present, if any, and the amount and form of water. A gas chromatograph/mass spectrometer, for measuring both atmospheric and surface composition, is being developed by JPL. The surface soil analyses will be directed at detecting evidence of growth and/or metabolism.

B. Space Sciences

1. Gas Chromatograph/Mass Spectrometer

a. Introduction. The gas chromatograph/mass spectrometer (GC/MS) is an automated instrument designed to perform a programmed number of Mars soil analyses and atmospheric analyses. The instrument will analyze Mars soil for its organic content by heating soil samples in pyrolysis ovens and introducing the resulting vaporized material into a gas chromatographic column that, in turn, is connected to a mass spectrometer. The heating of soil samples is to be accomplished in steps to vaporize those materials present that have sufficient vapor pressure, and ultimately to decompose pyrolytically nonvolatile substances to volatile degradation products from which the nature of the material can then be deduced.

In order to analyze materials not transmitted by the gas chromatograph, an additional pyrolysis oven is incorporated to vaporize material directly into the mass spectrometer. The instrument also incorporates the capability for admitting Mars atmospheric samples, with or without the removal of CO and CO_2, into the mass spectrometer for determination of atmospheric composition. The removal of CO and CO_2 is required in order to detect the presence of a small concentration of N_2 in the Mars atmosphere. The removal of CO and CO_2 reduces the background in the mass spectrum resulting from fragmentation and multiple ionization of these gases. The mass spectrometer incorporates dual electron beam voltage capability to permit discrimination of mass peaks produced by fragmentation.

b. Instrument capability and characteristics. The GC/MS instrument is 11 × 10 × 7 in. and weighs 23 lb. Its capabilities and characteristics are as follows:

Overall dynamic range. The GC/MS instrument is capable of analyzing soil samples containing from 5 to 5000 ppm volatile organic material, assuming that the volatile organic compounds, when separated from one another by the gas chromatograph, will be divided into one peak containing 80% of the volatile organic compounds and 100 peaks of equal size containing the remaining 20% of the volatile organic compounds. The evolution of large quantities of inert gases (up to 10% of the sample weight) will not incapacitate the instrument.

Soil analysis capability. The GC/MS is capable of analyzing eight Mars soil samples.

Atmospheric analysis capability. The GC/MS is capable of performing Mars atmospheric analyses on a noninterference basis with the soil analyses. An atmospheric analysis consists of six mass spectrometer scans with CO/CO_2 filters and six scans without filters.

Soil analysis data output. The GC/MS will provide the following data for each soil analysis:

(1) Maximum pyrolysis oven temperature.

(2) Gas chromatograph column temperature at 5-min intervals.

(3) A representation of the gas chromatogram.

(4) A mass spectrum from mass 12 to 200 for each gas chromatograph peak.

Atmospheric analysis data output. The GC/MS will provide a mass spectrum from mass 12 to 140 for each mass spectrometer scan during an atmospheric analysis.

Power consumption

(1) 65 W peak power and 50 W average power per soil analysis.

(2) 0.3 W-h per atmospheric analysis.

(3) 2 W during standby operation.

c. Functional description. A schematic representation of the GC/MS is shown in Fig. 1. The instrument is comprised of four functional subsystems:

(1) Soil sample pyrolysis.

(2) Gas chromatograph.

(3) Mass spectrometer.

(4) Instrument data.

The major functional elements in each subsystem are shown in Fig. 1. The functions and operational characteristics of each subsystem are as follows:

Soil sample pyrolysis subsystem. The soil sample pyrolysis subsystem receives soil material from the lander, loads the soil material into pyrolysis ovens, couples a loaded pyrolysis oven into the carrier gas line, vaporizes the soil material in the oven and injects the resulting effluent into the gas chromatograph for separation into constituent components.

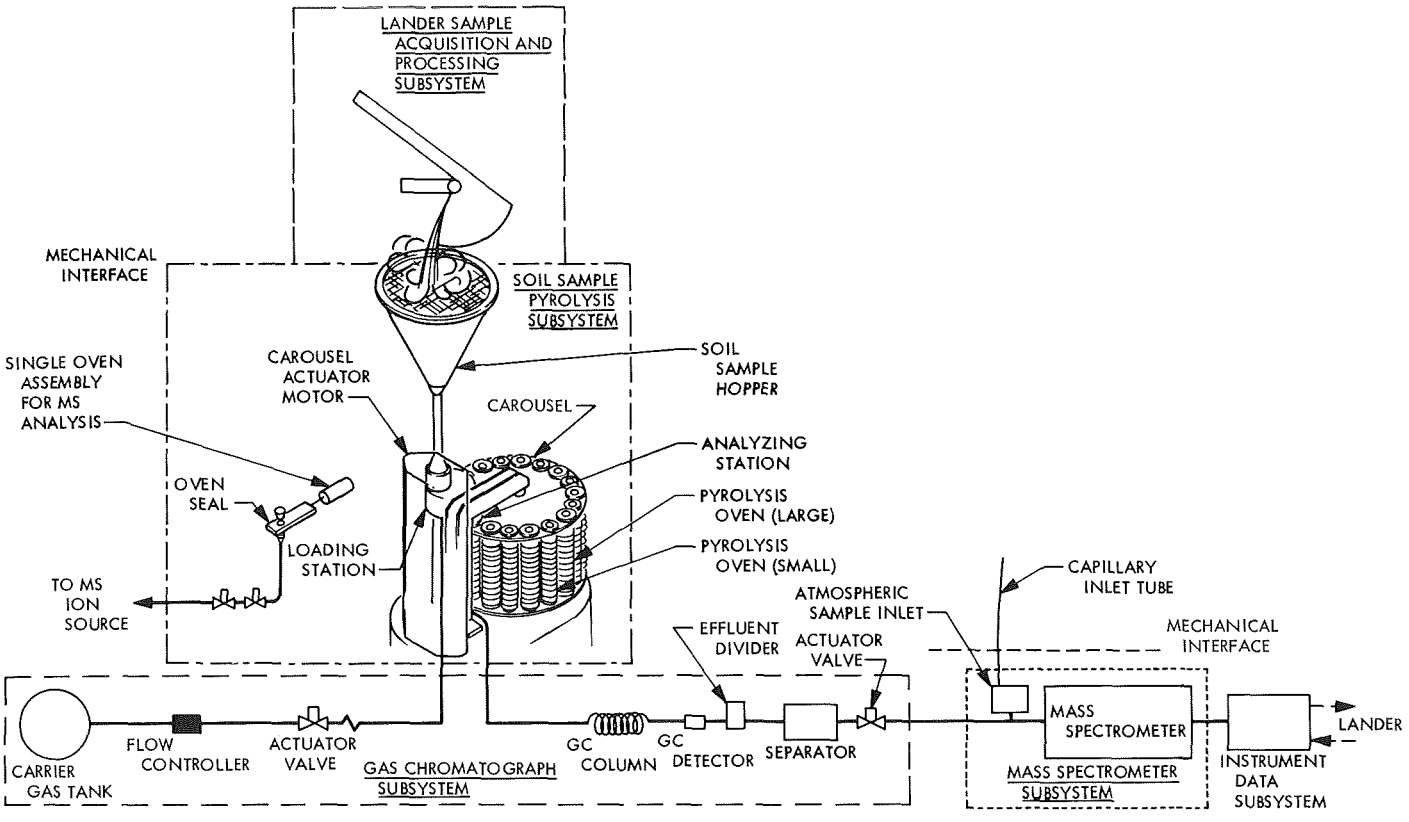

Fig. 1. Gas chromatograph/mass spectrometer schematic

This subsystem is comprised of a soil sample hopper, hopper full detector, oven loader, and sixteen pyrolysis ovens. The pyrolysis ovens are designed for flow-through effluent injection and are arranged in the form of a carousel with a station for loading of soil into the ovens and a station for analyzing the material in an oven. Two oven sizes, 25 and 250 mg, are available for analysis of each soil sample. Any two of three temperatures—150, 300, and 500°C—may be selected for sequentially analyzing the material in each oven.

In addition, the soil sample pyrolysis subsystem includes a 50-mg oven for vaporizing material directly into the mass spectrometer. The direct input oven may be heated to a maximum temperature of 500°C at a maximum heating rate of 20°C/min, or as slowly as necessary to prevent overload of the mass spectrometer.

Gas chromatograph subsystem. The gas chromatograph subsystem receives vaporized material from the pyrolysis ovens, separates this material into its constituent components, separates the carrier gas from the gas chromatograph column effluent, and introduces the remaining material into the mass spectrometer for analysis. In addition, the gas chromatograph subsystem protects the mass spectrometer from overload by detecting the presence of large quantities of inert gases in the effluent stream and venting these gases to the atmosphere. The gas chromatograph subsystem is comprised of a carrier gas tank, a chromatographic column, detector, effluent divider, and carrier gas separator.

The chromatographic column is a smooth-wall open-tube capillary, coated with SF96 Igepal. It has an efficiency of 50,000 theoretical plates based upon a hydrocarbon peak elution time of 30 min and can resolve the minor constituents in the test mixture of Table 1. The column can accept sample sizes between 0.01 μg and 1 mg with minimum alteration of its performance characteristics.

The gas chromatograph employs a cross-section detector with a Ni^{63} source. The detector sensitivity is on the order of 10^{-11} g/s. The detector output signal is sampled every 2 s during a soil analysis to provide a representation of the gas chromatogram. The detector output signal is also used to control the effluent divider. The effluent divider employs a variable conductance

Table 1. Chromatographic column test mixture

Compound	Volume %
CO_2	6.0
CH_4	1.7
H_2O	0.3
NH_3	0.5
NO	0.5
n-Butane	0.5
2-Methylfuran	
Acrylonitrile	
Benzene	
2.5 Dimethylfuran	
Mesitylene	
Undecane	
Indole	0.5
O-Cresol	
p-Cresol	
Hexadecene	
Hexadecane	
2-Aminophenylethane	
1-Phenylacetonitrile	
2-Hydroxymethylfuran	
H_2	90.0

vent located between the detector and the carrier gas separator. When the detector senses a concentration of inert gases or sample in excess of the established allowable limit, the vent conductance is increased and the overload is diffused into the atmosphere.

A palladium–silver tube is employed to separate the hydrogen carrier gas from the chromatographic column effluent. As the effluent flows through the tube, virtually all of the carrier gas diffuses through the wall of the tube. The remaining sample flows through the tube and into the mass spectrometer. The hydrogenation of certain compounds in the palladium separator and the effect of sulphide compounds on the separator have been investigated. Preliminary tests indicate that high concentrations of sulphides in the chromatographic column effluent temporarily decrease the separator efficiency; however, the separator completely recovered from the effects of sulphide poisoning within several minutes. Preliminary test results indicate high specificity of the hydrogenation reaction. The effects of compound alteration can be eliminated during data interpretation from a knowledge of chromatograph elution times and chemical reactivity.

Mass spectrometer subsystem. The mass spectrometer subsystem processes the gas samples from the gas chromatograph, direct pyrolysis oven, and the atmospheric inlet to provide mass spectrum data for identification of the constituents of the gas samples. The mass spectrometer subsystem is comprised of a gas sample inlet manifold, an atmospheric sample inlet, and a double focusing magnetic sector mass spectrometer.

The mass spectrometer is designed to scan the 12 to 200 mass range in less than 15 s with unit resolution or better, based upon a 10% valley definition for mass range 12 to 140 and a 20% valley definition for mass range 140 to 200. The mass spectrometer has a dynamic range of 10^5 and a sensitivity of 2.5×10^{-8} A/ng/s at 200 amu, assuming an electron multiplier current gain of 10^4. The mass spectrometer has a nominal electron beam energy level of 75 eV. A lower energy level in the 12 to 25 eV range may be selected by ground command.

The mass spectrometer incorporates a 1-liter/s ion pump integral with the mass analyzer to handle nominal sample gas loads. An additional 25 to 50 liters/s sublimation pump will be incorporated to handle gas overload transients. In the event of an overload, power to the ion source filament and the electron multiplier will be interrupted when the pressure inside the mass spectrometer increases to 10^{-5} torr and the sublimation pump will be turned on if the pressure continues to increase to 10^{-4} torr.

The atmospheric sample inlet incorporates a molecular leak to admit atmospheric samples into the mass spectrometer under molecular flow conditions. The sample inlet is designed to admit atmospheric samples directly into the mass spectrometer or through CO/CO_2 filters which remove 99% of CO_2 from the sample. The CO/CO_2 filtration is accomplished by chemically combining the atmospheric CO with I_2O_5 to convert the CO to CO_2. The CO_2 will then be eliminated by a LiOH or a NaOH filter.

Instrument data subsystem. The instrument data subsystem accepts coded commands from the lander for initializing analysis sequences, provides control signals for sequencing the instrument during an analysis cycle, processes the data produced by the instrument, and reads this data out to the lander for transmission to

earth. This subsystem incorporates a 4000-bit memory for temporary storage of mass spectrum data and a 300-bit buffer for temporary storage of instrument engineering data. The contents of both memories are read out periodically to the lander for transmission to earth. In addition, this subsystem incorporates circuitry for detecting and correcting up to two independent bit errors in commands received from the lander.

During a soil analysis the mass spectrometer is scanned continuously. The data from the latest complete scan plus additional data received during the time allowed for gas chromatograph peak detection and transmission delay is stored in the 4000-bit memory. If a gas chromatograph peak is detected, the elapsed time since the end of the last complete scan is checked to determine whether the current scan or the completed scan contains the maximum point of the peak. The data from the scan containing the maximum point of the gas chromatograph peak is transmitted to the lander. If a gas chromatograph peak is not detected, mass spectrometer scans will be transmitted at predetermined intervals, as established by ground command. In addition, scan initiation times and gas chromatograph peak detection times relative to the initiation of pyrolysis oven heating will also be sent to the lander.

The mass spectrometer peaks are quantized to a 9-bit logarithmic representation of peak magnitude. The full 9 bits are transmitted for each peak obtained during an atmospheric analysis. For soil analysis, the full 9 bits are transmitted for the base peak. The remaining peaks are compressed to a 4-bit representation of the ratio of each peak to the base peak. The mapping and resolution of soil analysis peak magnitudes in terms of the base peak ratio is shown in Table 2.

GC/MS engineering measurements and representations of the gas chromatograph spectrum, obtained by sampling of the gas chromatograph detector at 2-s intervals, will be stored in the 300-bit buffer for transmission to the lander. A partial listing of GC/MS engineering measurements is given below:

(1) Carousel position indication.

(2) Carrier gas-tank pressure and temperature.

(3) Carrier gas-reservoir pressure and temperatures.

(4) Pyrolysis oven temperature.

(5) Gas chromatograph column temperature.

(6) Gas chromatograph detector temperature.

Table 2. Mapping from 9-bit log $\frac{\text{base peak magnitude}}{\text{peak magnitude}}$ to 4-bit output word

Log $\frac{\text{base peak}}{\text{peak}}$	Top of range in binary notation	Output word	$\frac{\text{Peak}}{\text{Base peak}}$ ratio and resolution
0–5	000000101	1111	0.950 ± 0.050
5–10	000001010	1110	0.850 ± 0.050
10–15	000001111	1101	0.750 ± 0.050
15–22	000010110	1100	0.650 ± 0.050
22–29	000011101	1011	0.555 ± 0.045
29–37	000100101	1010	0.470 ± 0.040
37–45	000101101	1001	0.395 ± 0.035
45–54	000110110	1000	0.325 ± 0.035
54–64	001000000	0111	0.260 ± 0.030
64–77	001001101	0110	0.200 ± 0.030
77–93	001011101	0101	0.145 ± 0.025
93–110	001101110	0100	0.100 ± 0.020
110–130	010000010	0011	0.065 ± 0.015
130–160	010100000	0010	0.0375 ± 0.0125
160–200	011001000	0001	0.0175 ± 0.0075
200–300	100101100	0000	0.0055 ± 0.0045
300 up		not saved	0.001 down

(7) Ion source filament current.

(8) Mass spectrometer scan voltage.

(9) Ion source temperature.

(10) Mass spectrometer deflection plate voltages.

(11) Electron multiplier voltage.

(12) Ion pump current.

d. Science breadboard tests. Since the completion of the GC/MS science breadboard, a series of engineering and science tests have been conducted in order to demonstrate the performance capability of the breadboard instrument. The test plan included: atmospheric gas analysis test; organic analysis tests consisting of the injection, volatilization, and pyrolysis of selected compounds and mixtures; engineering tests to verify component and system parameters; and the utilization of the science breadboard system as a test-bed for the continued development of components required in the engineering breadboard.

Tests were designed to demonstrate the ability of the science breadboard instrument to produce acceptable scientific data. These data include total ionization monitor gas chromatograms of injected and pyrolyzed mixtures and mass spectra corresponding to the various gas chromatographic fractions. Descriptions of these tests follow.

A mixture of furan, methylfuran, methylcyclohexane, benzene, and toluene was injected on a 0.006-in. ID capillary column coated with SF96 Igepal. The chromatogram showed complete resolution of these components with a column temperature of 50°C, and the corresponding mass spectra were comparable to reference spectra.

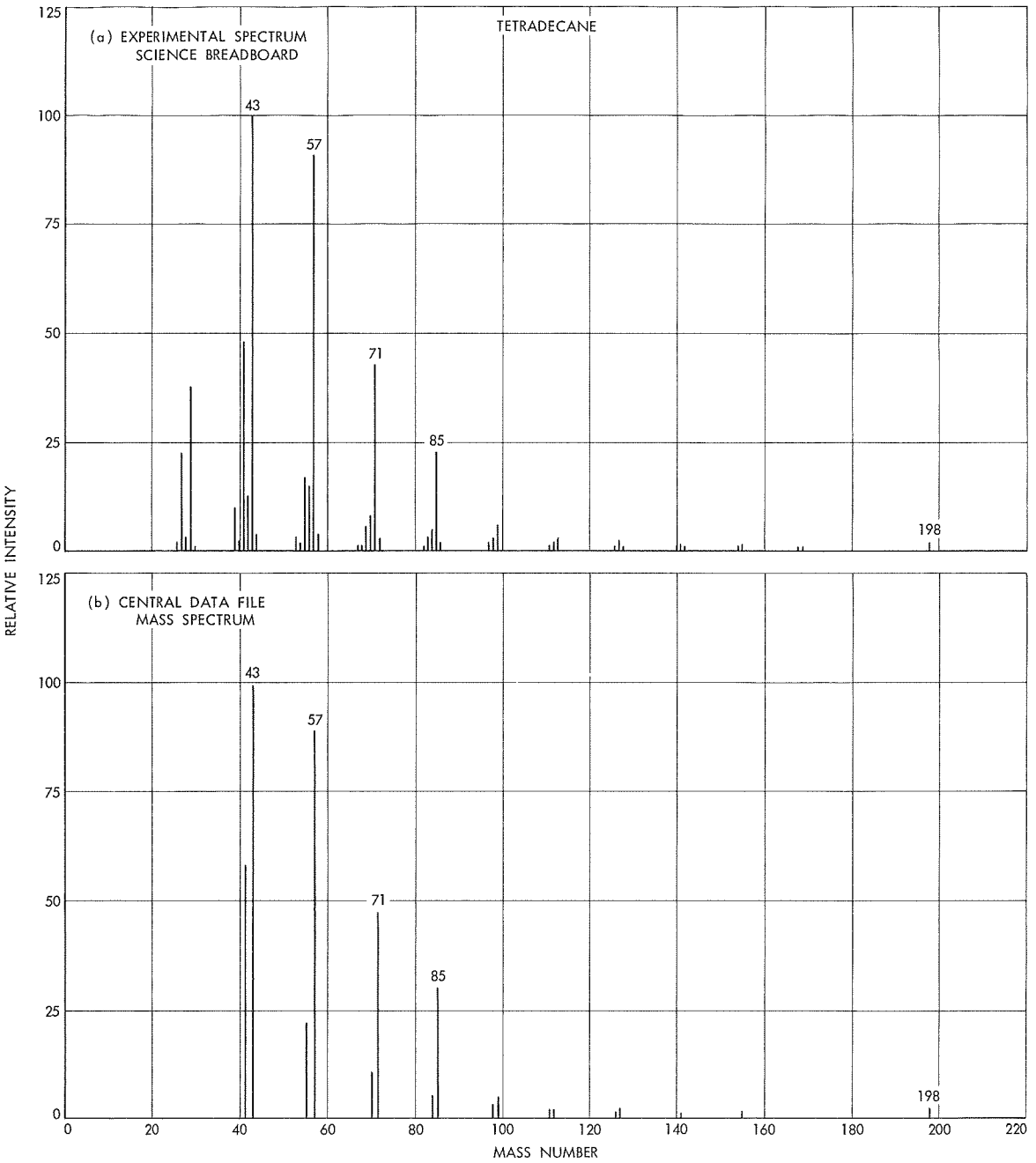

Fig. 2. Tetradecane mass spectrum: (a) experimental science breadboard, (b) central data file

A mixture of nonane, undecane, and tetradecane was injected on this column. The resultant chromatogram and the mass spectra of all components showed a good correlation to published spectra. The experimental mass spectrum of tetradecane is compared to a reference spectrum in Fig. 2. Note the similarity of the pattern through the entire mass range.

A mixture of furan, furfural, pyrrole, and dimethylsulfoxide was injected on the 6-mil column. The chromatogram showed good separation of all components, and the mass spectra were acceptable. The experimental and reference spectra of furfural and pyrrole are shown in Figs. 3 and 4. It is important to note that the dimethylsulfoxide passed through the palladium separator

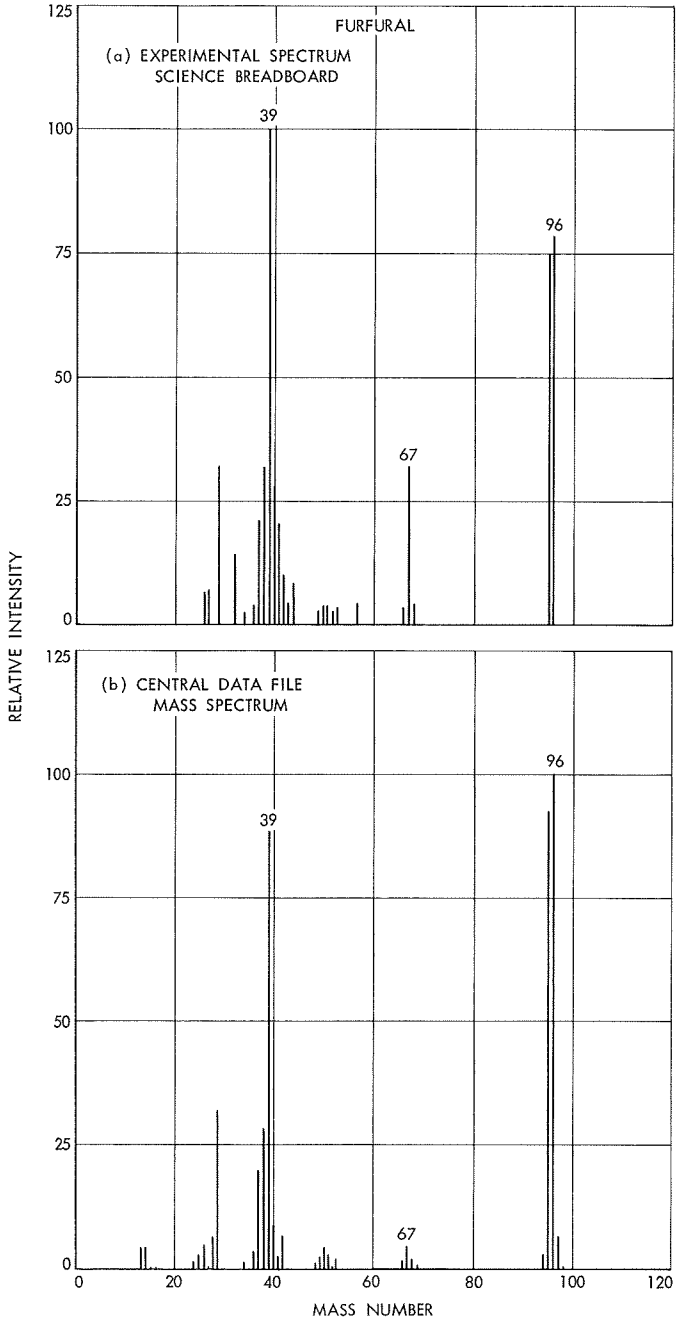

Fig. 3. Furfural mass spectrum: (a) experimental science breadboard, (b) central data file

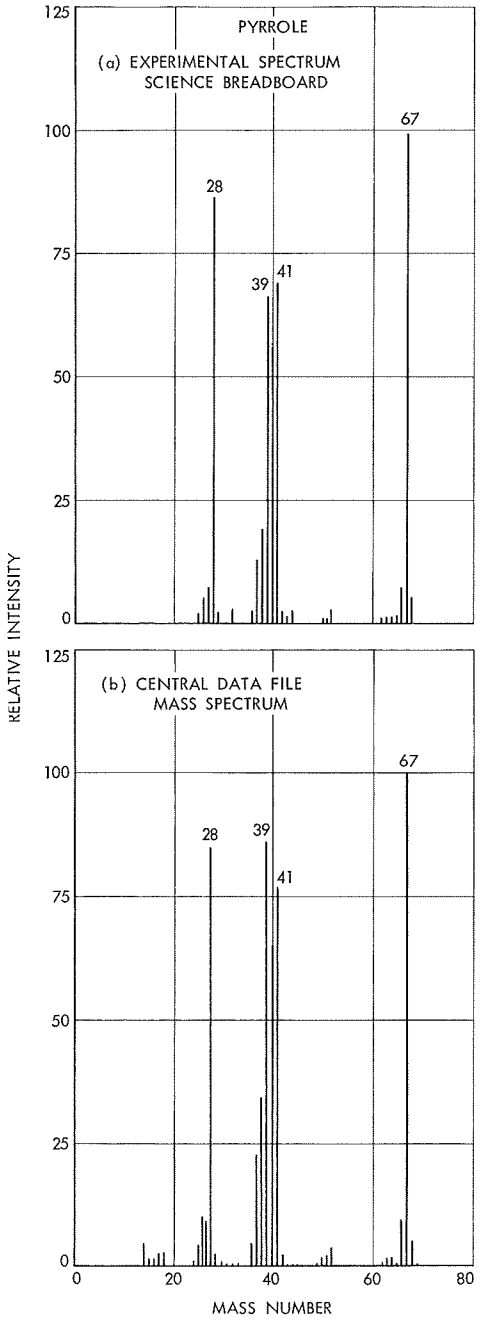

Fig. 4. Pyrrole mass spectrum: (a) experimental science breadboard, (b) central data file

and at the concentration levels used (equal amounts of all compounds) there were no adverse effects observed as a result of the possible sulfur–palladium interaction.

Phenylalinine was coated on glass beads and pyrolyzed onto the 6-mil column. The gas chromatogram and mass spectra indicated that the major pyrolysis products were benzene, toluene, ethylbenzene, and styrene. This corresponds to results published by Shulman and Simmonds (Ref. 1).

The following tests were conducted on a 0.020-capillary column which was operated isothermally at 150°C and coated with SF-96. A cross-section detector was added to the system between the column and separator.

The injection of furan, methylfuran, methylcyclohexane, benzene, and toluene gave a good gas chromatogram and good mass spectra. The pyrolysis of phenylalinine gave results similar to those reported above. The cross-section detector operated as expected.

A mixture with the following components was prepared: benzene, heptanal, 1,3,5-trimethylbenzene, phenylacetate, benzyl alcohol, N-methylaniline, undecane, and methyldecanoate. Both an injection and a pyrolysis of this mixture gave chromatograms showing the expected number of fractions. Mass spectra of these fractions corresponded to reference spectra of the above components.

The science breadboard is operating as a functional GC/MS. We have demonstrated the ability to volatilize and pyrolyze representative organic mixtures and generate the appropriate gas chromatograms and mass spectra. The results obtained show good correlation with data generated by laboratory instruments.

Reference

1. Shulman, G. P., and Simmonds, P. G., *Chem. Comm.*, 1968, p. 1040.

C. Guidance and Control

1. Orbiter Power Subsystem

a. Power requirements. During this reporting period a reduction of the *Viking* orbiter power requirements has been achieved. A major reduction occurred in the *Viking* lander whereby the use of the primary power source (radioisotope thermoelectric generator) has reduced the demand from the orbiter by approximately 60%. The selection of a lower battery charging rate of C/15 as compared to the C/10 rate discussed in the orbiter baseline design (SPS 37-56, Vol. I, pp. 42–47) has reduced the raw battery charging power by approximately 30%. Battery energy requirements have increased by approximately 10 W-h. A summary of the latest total power requirements is shown in Table 3.

b. Solar panel. The rationale for sizing of the solar panels has been based on an operational mode requiring an orbiter battery charging and science playback mode in combination with the lander power demand at a point in time of 50 days after the orbit insertion maneuver (OIM)—March 20, 1974—or May 10, 1974. On this date the specific solar panel performance is estimated to be approximately 3.6 W/ft^2. This is a deviation from the specific performance discussed in the previous reporting period (SPS 37-60, Vol. I, pp. 36–37). The reduction of approximately 0.5 W/ft^2 is due primarily to the results of a more rigorous thermal analysis as well as the correlation of the *Mariner* Mars 1969 flight performance to the expected *Viking* performance. On the basis of the revised power profile and projected panel performance, a gross solar panel area of 158 ft^2 equally divided into six panels and providing 570 W is contemplated at the present time. A preliminary functional block diagram of the *Viking* orbiter power subsystem depicting the six-panel configuration is shown on Fig. 5.

c. Battery charging. Because of the desire to reduce the orbiter power demand, the *Viking* Project has selected a lower battery charge rate (C/15) in lieu of the C/10 rate discussed in the baseline design. However, the decrease in raw power, approximately 41 W, requires a longer charging period. The charging time is directly associated with the effect of cell temperature.

A comparison of charging time for 70 and 90°F temperature levels in combination with the C/15 rate is shown in Fig. 6. Considering the orbit insertion maneuver load and the 70°F battery cell temperature level, one battery may be charged to approximately 95% of full capacity in about 15 h. In the remaining hours prior to the next sun occultation mode, the second battery will be recharged to approximately 75 to 80% of full capacity.

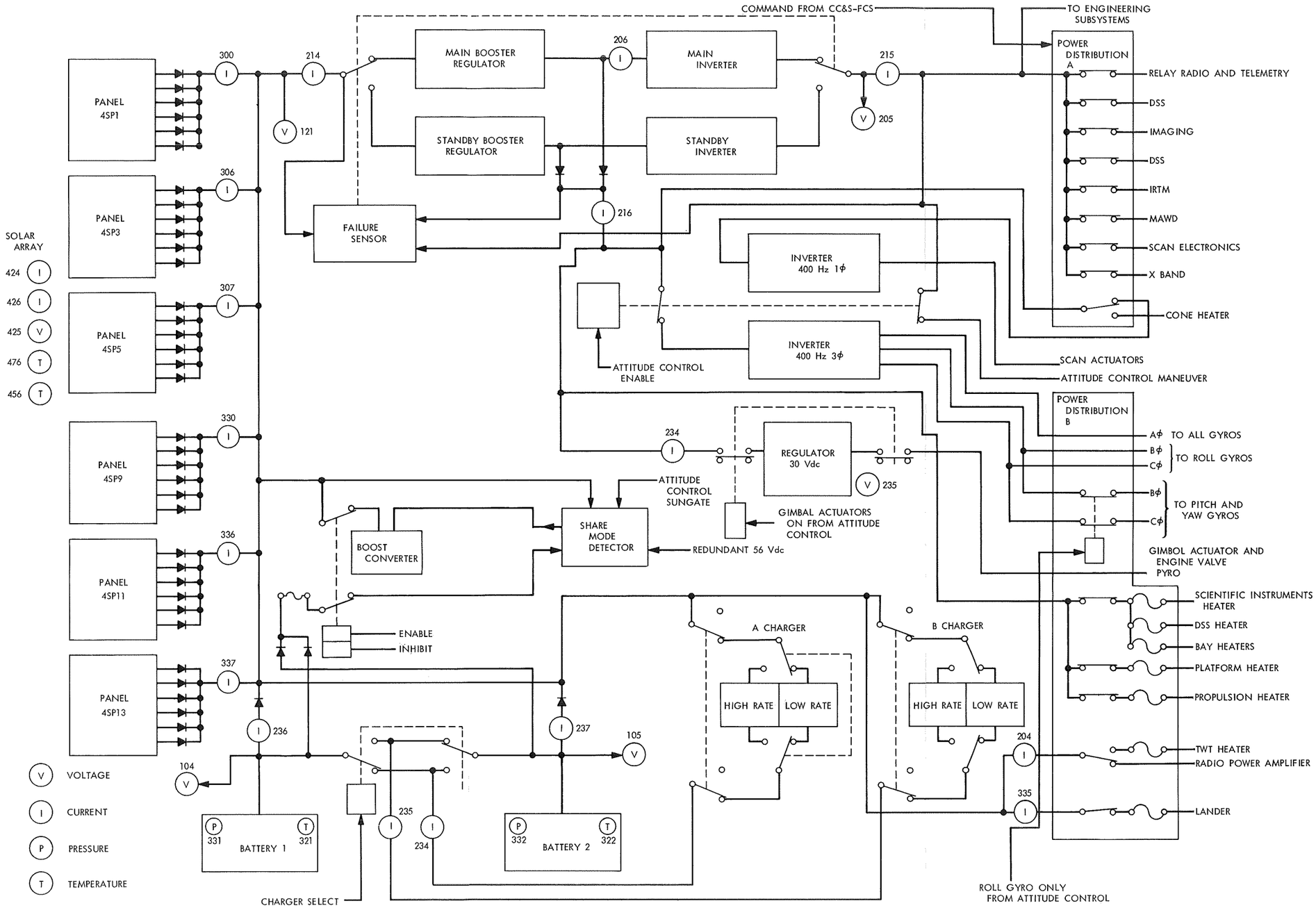

Fig. 5. *Viking* orbiter power subsystem

Table 3. Preliminary *Viking* orbiter power profile

Operational mode	Power required, W	Power source
1. Launch	514	Battery
2. Sun acquisition	437	Battery
3. Canopus acquisition	434	Solar panel
4. Cruise—high rate charger on (gyros off)	478	
5. Cruise—low rate charger on (gyros off)	421	
6. Cruise—lander TWT checkout	496	
7. Trajectory correction	521	Battery
8. Maneuver turns for orbit insertion	308	
9. Orbit insertion burn	361	
10. Sun occultation—orbit insertion maneuver (OIM)	284	
11. Post OIM, battery charge	478	Solar panel
12. Cruise low rate trickle charge	424	Solar panel
13. Cruise science on, lander attached	519	Solar panel
14. Sun occultation with lander	442	Battery
15. Post sun occultation, high rate charge, science playback	495	Solar panel
16. Post-orbit cruise, low rate charge, science playback	437	
17. Orbit cruise—lander preseparation checkout S — 19 h to S — 2.5	428	
18a. Orbit cruise—lander preseparation checkout (gyro warmup)	449	
18b. Orbit cruise—lander preseparation checkout 30 min on	873	Solar panel/ Battery
18c. Orbit cruise—lander preseparation checkout 70 min on	779	Solar panel/ Battery
19. Orbit cruise—lander entry	372	Solar panel
20. Orbit cruise—low rate charge, lander detached	379	
21. Periapsis pass—science on, relay off	494	
22. Orbit cruise—orbiter science on, relay off	474	
23. Sun occultation—lander detached	397	Battery
24. Orbit cruise—high rate charge, lander detached	433	Solar panel

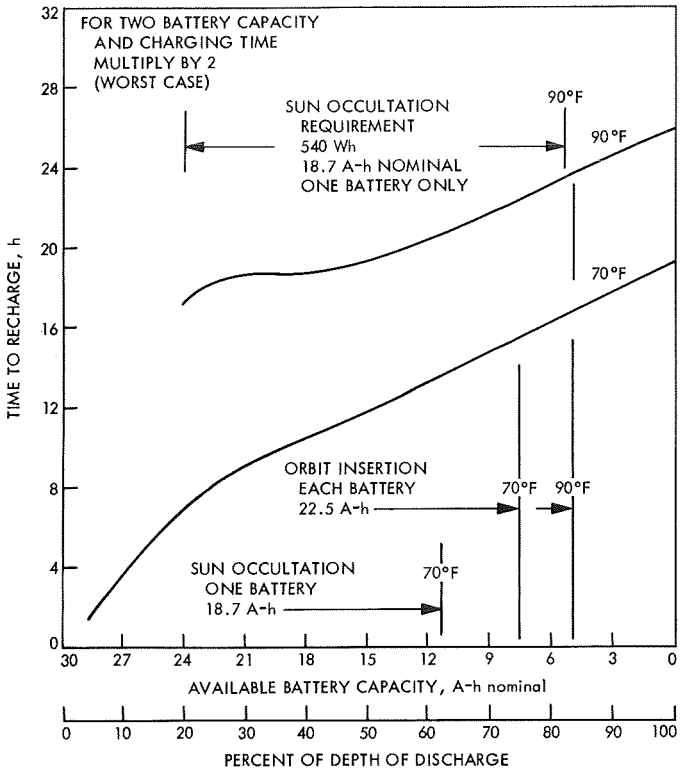

Fig. 6. Battery charging time at 70 and 90°F with C/15 charge rate

However, at the 90°F cell temperature the first battery will be charged to approximately 80% of full capacity in about 23 h. At this temperature level and charge rate, the instantaneous ampere-hour efficiency approaches zero at 80% of full charge. Charging for longer periods of time cannot overcome the charging efficiency losses due to rise in temperature. The data used to derive the above information has been extrapolated from early testing of the *Mariner* Mars 1971 20-A-h Ni-Cd cell. During the first quarter of 1970 the *Viking* orbiter 30-A-h cell will be available for testing.

d. Subsystem weight. The increase in power requirements for both the orbiter and lander required a 6.15% increase in the overall subsystem weight. The latest status of the subsystem weight is summarized in Table 4.

e. Telemetry channel assignments. A tentative power subsystem telemetry channel assignment has been established. Additional assignments over that of the previous *Mariner* series spacecraft are due primarily to the requirement of two additional solar panels, one additional battery and the lander. A summary of a tentative list of telemetry assignments is shown in Table 5. These assignments are also shown on Fig. 1.

Table 4. Preliminary power subsystem weight

Unit	Weight (estimated design), lb	Deviation from baseline design, lb
Solar cells, coverslides (active area 142.2 ft² not including substrate) Packing factor 90%	63.2	−6.48[a]
Batteries—Ni Cd (2) (Including case weight)	152.0	+14.00
Battery charger (2)	6.5	−2.5
2.4-kHz Inverter (2)	10.0	+4.0
Booster regulator (2)	15.0	+3.0
Power control	3.5	+1.2
Power source logic	10.0	+2.0
400-Hz inverter	3.5	0
Dc/dc regulator	4.5	−1.5
Heater—lander dc power distribution	3.0	+1.0
Power distribution	3.0	+1.17
Total	274.2	+15.89

[a]The decrease in solar cell weight is due to the use of the 14-mil cell and 6-mil coverslide.

Table 5. Tentative power subsystem telemetry functions

Deck	Function	Range
104	Battery 1 voltage	0–3 V
105	Battery 2 voltage	
121	Power source and logic output voltage	
204	Power source and logic current to RFS	
205	2.4-kHz Inverter output voltage	
206	2.4-kHz Inverter input current	
214	Boost regulator input current	
215	2.4-kHz inverter output current	
216	400-Hz input current	
234	Battery charger A output current or 30-V regulator input current	
235	Battery charger B output current or 30-V regulator output voltage	
236	Battery 1 output current	
237	Battery 2 output current	
300	Bay 1 solar panel current	
306	Bay 3 solar panel current	
307	Bay 5 solar panel current	
315[a]	Power status monitor	Digital
321	Battery 1 temperature	500–600 mV
322	Battery 2 temperature	500–600 mV
330	Bay 9 solar panel current	0–3 V
331	Battery 1 pressure	
332	Battery 2 pressure	
335	Lander current	
336	Bay 11 solar panel current	
337	Bay 13 solar panel current	
424	Standard cell current	0–100 mV
425	Standard cell voltage	0–100 mV
426	Radiation resistance cell current	0–100 mV
444	Power regulator bay temperature	500–600 mV
456	+X Solar panel temperature	
464	Power converter bay temperature	
476	−X Solar panel temperature	

[a]See Table 6.

2. Radiation Effects of the *Viking* Lander Radioisotope Power System on the Orbiter

a. Introduction. The *Viking* lander will be powered by two radioisotope thermoelectric generators (RTGs) fueled with 675 W(th) of plutonium-238 each. The plutonium will be in the form of plutonium dioxide, and will contain sizable amounts of other plutonium isotopes, including about 1–2 ppm of plutonium-236. The decay chain of the plutonium-236 produces a significant amount of gamma radiation (SPS 37-59, Vol. III, pp. 112–115). The (α, n) reactions involving the oxygen-18 isotope are responsible for most of the neutrons produced by the fuel. The radiation characteristics of the fuel have been described in SPS 37-56, Vol. III, pp. 128–132.

The radiation field produced by the RTG on the space vehicle can lead to erroneous scientific measurements (SPS 37-60, Vol. III, pp. 88–98) and to degradations in solid-state electronics, solar cells, optical lenses and coatings, and other components. This article briefly discusses progress made to date in defining these problems on the *Viking* orbiter.

b. Determination of the radiation fields on the Viking orbiter. The radiation field around the *Viking* orbiter has been calculated (SPS 37-60, Vol. I, pp. 33–36) using Monte Carlo computer techniques (Ref. 1; SPS 37-44, Vol. IV, pp. 24–27; and SPS 37-49, Vol. III, pp. 81–91).

Table 6. Tentative power status monitor assignment (channel 315)

Bit 1	Battery A charger *on/off*
Bit 2	Battery A charger *hi/low*
Bit 3	Battery B charger *on/off*
Bit 4	Battery B charger *hi/low*
Bit 5	Booster converter *inhibit/enable*
Bit 6	Battery charger A *inhibit*
Bit 7	Battery charger B *inhibit*

These calculations include only the shielding effects of the reentry capsule of the RTGs, not the RTGs themselves or the other structural parts of the space vehicle. The results were based on newly processed fuel as well as 1- and 5-yr-old fuel to include the effect of composition (and hence radiation) changes produced by the decay chains. The results on the newly processed fuel seem to correspond closely with results obtained informally from the Martin Marietta Corp. These radiation results are being used to determine the seriousness of radiation problems on the orbiter and to plan radiation tests on specific components.

c. Radiation tests on space vehicle components. A number of radiation tests are already in progress. Neutron exposure tests are being performed at Battelle Memorial Institute, and gamma radiation tests are being performed inhouse (SPS 37-59, Vol. III, pp. 124–127). In February 1970 the JPL gamma irradiation facilities will be enhanced with the addition of a cobalt-60 source, and conversion work on the JPL Dynamitron will allow all neutron tests to be performed on-Lab, hopefully early in 1970.

Neutron irradiation tests have already been conducted on solar cells, a Canopus sensor, and a gyroscope. The test results are still being evaluated. In the near future, the Canopus sensor will also be exposed to gamma rays. No gamma ray tests are contemplated on the solar cells; for the gyroscope these tests have already been performed. The propulsion and the pyrotechnic subsystems are presently being examined to define and plan necessary tests.

Reference

1. Gingo, P. J., *Radiation Mapping of a Planetary Surface Lander System*, Technical Report 32-1252. Jet Propulsion Laboratory, Pasadena, Calif., April 15, 1968.

3. Thrust Vector Control Considerations for Three-Engine Propulsion System Option

a. Introduction. The thrust vector control (autopilot) and propulsion systems for the current *Viking* orbiter baseline are essentially minimum modifications from the *Mariner* Mars 1971 design. To eliminate the long orbit-insertion burn duration and a major part of the gravity losses that are inherent with this design, an alternate option employing three 300-lbf gimballed liquid bipropellant engines was considered. This report summarizes the results of a preliminary study that was made to determine the thrust vector control implications of such a system.

b. Engine configuration. From the standpoint of thrust vector control, the following general comments can be made when multiple-gimballed engine configurations are compared with the single-gimballed engine baseline design:

(1) Sensitivity to initial c.m. offset errors is more pronounced, due to higher resultant thrust level and inherent slow response of gimbal actuator control systems. This increased sensitivity degrades transient response.

(2) Variations in start-up and shut-off times between engines degrade transient behavior.

(3) Unless some form of path guidance compensation is utilized, variations in engine steady-state thrust levels which produce a steady-state disturbance identical in effect to a c.m. offset can significantly degrade steady-state pointing accuracy.

(4) Lower shut-off accuracy with regard to ΔV magnitude.

(5) Greater number of mechanical alignment and engine geometry error sources.

(6) Lower reliability due to additional autopilot electronics and gimbal actuators.

Several mechanizations exist for a three individually gimballed engine configuration. It is assumed that one engine is mounted coincident with the vehicle roll axis and that the remaining two are located outboard parallel to the X axis with their thrust directions parallel to the center engine. Some of these mechanizations are:

(1) Two-axis gimballing of center engine for pitch-yaw control with single-axis gimballing of outer two engines such that they provide a torque couple for roll control.

(2) Same as (1), except that just one outboard engine is gimballed for roll control.

(3) Two-axis gimballing of center engine and one outboard engine for three-axis control.

(4) Two-axis gimballing of all three engines for three-axis control.

In all of the above alternates, it is desirable to use only the center engine for the small ΔV maneuvers (midcourse and orbit trims). During these maneuvers, roll control would be provided by the cold gas system.

The first configuration listed above was selected as the most feasible on the basis of symmetry and mechanization complexity. A diagram showing the engine location and gimballing relative to spacecraft coordinates is given in Fig. 7.

c. Accuracy considerations. As previously stated, the basic pointing accuracy of a three-gimballed engine system is less than a single-engine system if conventional thrust vector control is used. Figure 8 shows the system behavior for a c.m. offset. If thrust levels are considered to be identically equal and all alignment errors are zero, the steady-state torque equation is

$$T(L + \delta) - T(L - \delta) + T\delta - T\phi d_1 = 0 \qquad (1)$$

where

δ = c.m. offset, ft

d_1 = center engine gimbal lever arm, ft

The required gimbal deflection ϕ of the center engine to maintain control is then

$$\phi = \frac{3\delta}{d_1}$$

where δ/d_1 is the initial angular misalignment of the center engine with the c.m. This gimbal deflection is exactly three times as much as would be required for single engine control. Considering an X or Y c.m. offset, the steady-state thrust vector relative to spacecraft coordinates can be expressed as

$$\mathrm{T} = |T|\,(2 + e^{j\phi}) = |T|\,(2 + \cos\phi + j\sin\phi) \qquad (2)$$

where the gimbal deflection of the outer engines and their misalignment errors are considered negligible compared to ϕ. The thrust vector pointing direction relative to spacecraft coordinates is then

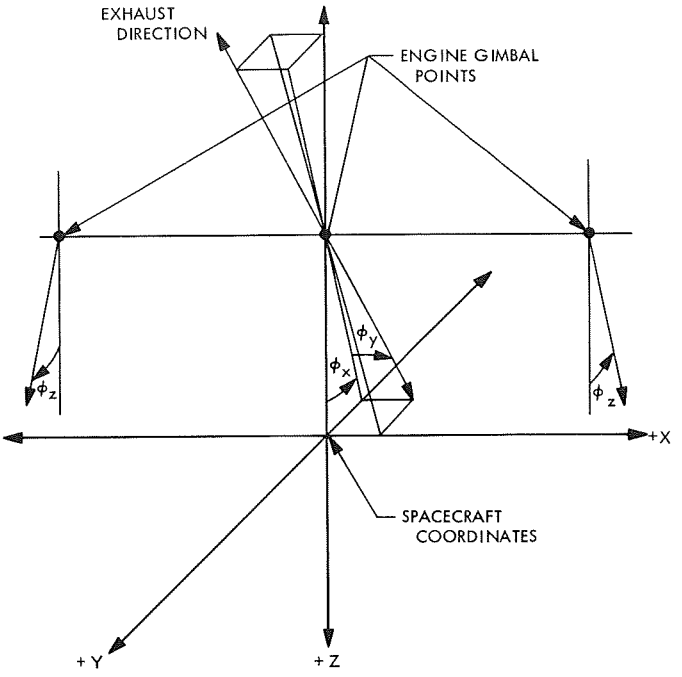

Fig. 7. Gimbal angle definition

$$\phi_{ss} = \tan^{-1}\left(\frac{\sin\phi}{2 + \cos\phi}\right) \approx \frac{\phi}{3} \qquad (3)$$

Since the gimbal servo derives its input signal from the gyro error signal, the spacecraft will assume a steady-state angular error in inertial space. This, of course, assumes no path guidance correction. The total thrust vector pointing error in inertial space for a c.m. offset is

$$\alpha_{ss} = \frac{1}{K_f}\left(\frac{3\delta}{d_1}\right) + \alpha_{sc} \qquad (4)$$

$$= \frac{\delta}{d_1}\left(1 + \frac{3}{K_f}\right) \qquad (5)$$

where

K_f = autopilot forward loop gain between gyro input and gimbal angle output

The equivalent error expression for a single-engine system is

$$\alpha_{ss1} = \frac{\delta}{d_1}\left(1 + \frac{1}{K_f}\right) \qquad (6)$$

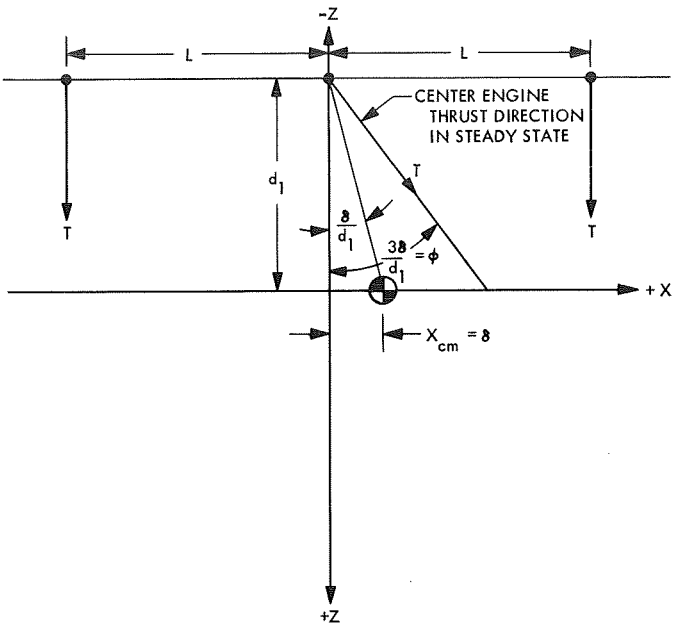

Fig. 8. System behavior to c.m. offset

An approximate but more general expression than Eq. (5), which accounts for steady-state thrust magnitude errors, engine misalignment errors, and c.m. offsets can be derived in a similar manner:

$$\alpha_{ss} = \left[\frac{1}{d_1}\left(\frac{(\Delta T_{out})L}{T_{nom}} + 3\delta\right) + \alpha_1 + \alpha_2\right]\left(\frac{1}{K_f} + \frac{1}{3}\right) + \alpha_T + \alpha_E \quad (7)$$

where

ΔT_{out} = magnitude of steady-state thrust variation between outboard engines, lb

α_1, α_2 = angular misalignment of outboard engines

α_T, α_E = center-engine angular misalignment errors

T_{nom} = nominal thrust of a single engine

Inspection of Eq. (7) shows that outboard engine steady-state thrust level variations and outboard engine alignment errors affect steady-state pointing error in the same manner as a c.m. offset. Center-engine alignment errors directly influence steady-state pointing error. As an example, consider the following case:

$d_1 = 4.11$ ft

$T_{nom} = 300$ lbf

$\Delta T_{out} = 30$ lb (corresponds to +5% and a −5% variation in outboard engine thrust levels)

$L = 2$ ft

$\delta = \frac{1}{4}$ in. $= 0.0208$ ft

$K_f = 3.134$

$\alpha_1, \alpha_2, \alpha_T, \alpha_E = 0$

Substituting the above values into Eq. (7) yields

$$\alpha_{ss} = 2.39 \text{ deg}$$

The pointing error for a single engine system under the same conditions would be, from Eq. (6):

$$\alpha_{ss1} = 0.38 \text{ deg}$$

Referring to Eq. (7), it is seen that the error terms representing c.m. offset, outboard engine thrust level variation, and outboard engine alignment errors are modified by a term containing the autopilot forward loop gain $(1/K_f + 1/3)$. If this term can be set equal to zero, then the three-gimballed engine system is competitive with the single-engine baseline system from the standpoint of autopilot pointing accuracy. Setting this term to zero amounts to requiring that the autopilot forward loop gain between gyro input and gimbal angle output be set equal to -3 $(K_f = -3)$. This condition can be mechanized using the same type of path guidance scheme that is proposed for the single-engine baseline design. The pointing accuracy of this system is then theoretically the same as the single-engine design, where the only remaining source of error (which cannot be compensated for) is the center-engine alignment errors.

A second area of concern with regard to system accuracy, is the effect of variations in impulse between engines at start-up and shut-off (thrust tail-off). In particular, system performance is more sensitive to impulse variations during tail-off than during the start-up transient, since any one-sided impulse that is present during tail-off must be corrected by the cold gas system. The maximum allowable impulse error during this time is determined by the available gyro integrator angular storage capability. The current design provides six degrees of integrator angular storage. A certain amount of this available storage, depending on such errors as thrust level variations and c.m. offsets, will always be required for path guidance compensation. Taking this factor into

account, preliminary considerations indicate that a reasonable upper bound on engine-to-engine impulse variation during thrust tail-off should be ±7.0 lb-s.

d. Computer simulation. A preliminary design of the three individually gimballed engine autopilot was made to assess its performance and to investigate the major problem areas associated with its use for the *Viking* orbiter. The analysis was facilitated through the use of a six-degree-of-freedom autopilot and spacecraft dynamics simulation program written specifically for this purpose. It should be noted that the preliminary design was not optimized but rather carried to the point where major problem areas can be identified and basic overall system performance can be evaluated.

Figure 9a shows the velocity vector pointing error as a function of time for the previous example. In the simulation, the engine is ignited at $t = 2.0$ s and burns for 50 s. Steady-state pointing error is 2.29 deg. This value is in close agreement with the value predicted by the approximate pointing error equation (Eq. 7) previously derived. It should be noted that this error plot represents only autopilot, thrust level, and c.m. alignment errors and does not include any other, such as turn errors or maneuver execution errors. If some form of path guidance correction is not utilized, the basic accuracy of this type of system is significantly lower than the single-engine baseline system.

Figure 9b shows pointing error for the three-engine system with the inclusion of path guidance compensation. The path guidance parameters and autopilot forward loop gain were set according to the criteria set forth under accuracy considerations in this article. This simulation is based on the following conditions:

(1) C.M. offset = −¼ in. along negative yaw axis.

(2) Variation of +5% in thrust level on center engine and one outboard engine, −5% variation on remaining outboard engine thrust level.

(3) Alignment error of ½ deg on outboard engines such that disturbance torque is additive to the c.m. offset disturbance.

All of the above sources of error can be corrected for by proper path-guidance compensation in the center-engine pitch-and-yaw-control channels. Figure 9b shows the path-guidance reduction in pointing error as the burn progresses. If these were the conditions at orbit insertion, pointing error (for the above error sources) would be essentially zero by the end of the burn (15 min).

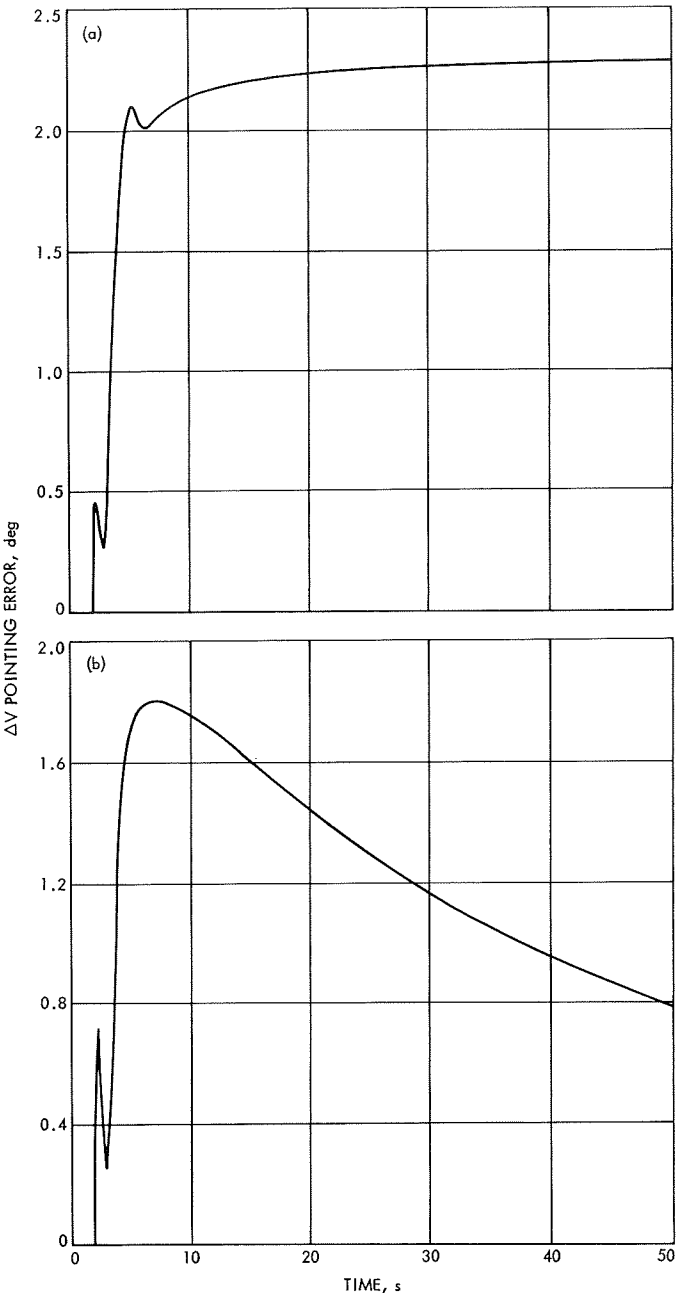

Fig. 9. ΔV pointing error versus time: (a) no path guidance compensation, (b) with path guidance compensation

As previously stated, the design of this system was not optimized, but rather carried to the point where basic system behavior can be examined. The analysis for the autopilot, as presently conceived, indicated that additional compensation is needed to provide adequate stability margins. In addition, due to its nonlinear nature, the system is extremely sensitive to initial conditions. This characteristic is dramatically shown in Fig. 10. The

instability was created by placing the c.m. 0.5 in. along the negative pitch axis and introducing a ±5% variation in engine steady-state thrust levels such that the resulting yaw disturbance torques are additive. The resultant yaw axis disturbance is sensed by the yaw gyro, which for this case produces an error signal that is sufficiently large to cause electrical saturation (12 V) on the output of an operational amplifier within the autopilot compensation electronics. This saturation condition produces, in effect, an open-loop condition within the autopilot yaw channel. The result is mechanical saturation of the yaw gimbal (9 deg). This results in a divergent or unstable behavior within the autopilot and in vehicle attitude. Although this set of initial conditions may seem extreme, they are roughly equivalent in total to a pitch axis c.m. offset of 1 in. Considering all the sources of error a system of this type has, a total error equivalent to this much c.m. offset is not unreasonable. This situation, however, could be greatly improved through optimization of the autopilot parameters, additional compensation, and greater gimbal travel on the center engine.

e. Conclusion. The results of the preliminary analysis and computer simulations indicate that a realizable autopilot control system for a three individually gimballed engine propulsion system could be mechanized. The following conclusions are based on this analysis:

(1) A three-gimballed engine autopilot mechanization should employ path-guidance compensation in order to be competitive with the single-engine mechanization due to the greater number of error sources.

(2) The autopilot mechanization will be more complex and less reliable than the single-engine design as a result of an additional autopilot channel and additional actuators.

(3) Engine mechanical alignment tolerances and engine impulse variation, particularly during thrust tail-off, should be held tighter in comparison to *Mariner* Mars 1971 or the *Viking* baseline mechanization. Impulse variations between engines during tail-off must be held to within ±7 lb-s.

(4) Sensitivity to errors which behave like c.m. offsets is increased. This effect reduces the system overall stability margin.

(5) Accuracy of the ΔV magnitude will be lower, due to the shut-off inaccuracies of three engines.

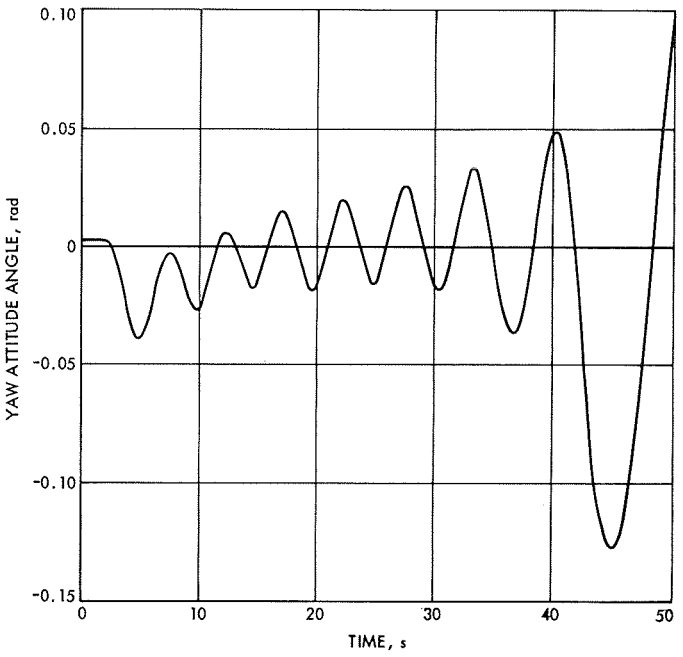

Fig. 10. Path guidance compensation instability from initial conditions

D. Engineering Mechanics

1. Insulation Materials for Mars Lander Application

Early Mars lander studies indicated that thermal insulation material performance was a key uncertainty area. Most performance data available were for either vacuum environment or atmospheric conditions. Without sufficient performance data for all phases of the mission, sufficient thermal insulation would have to be included to provide for all possible contingencies, resulting in a prohibitive lander weight. Thus, a study was instituted at McDonnell Douglas Astronautics Co. to obtain the required data.

Test criteria were selected on the basis of the environmental parameters most pertinent to insulation material performance, specifically: heat sterilization (135°C for 65 h in dry nitrogen for six cycles), launch venting and vibration, landing shock, and exposure to the Mars surface environment. Approximately 25 materials of four classes (fibers, foams, powders, and multilayer materials) were selected for the initial screening tests.

Thermal diffusivity tests were conducted at ambient temperature (75 ± 5°F) and pressures of 10^{-4} torr (vacuum), 20 mbar, and 1 atm to compare the thermal conductivities of the candidate materials. To establish the

heat-sterilization compatibility of the materials, thermogravimetric analysis, differential thermal analysis, and effluent gas analysis were performed by heating the samples to 235°C (100°C above the heat-sterilization temperature) at 1-atm pressure.

Based on the results of these tests, two materials—Upjohn HTF-200 Isocyanurate foam and Johns-Manville silicone bonded AA fiberglass—were selected for insulation system module testing. These tests were to include dry-heat sterilization, vibration, shock, launch pressure profile, and system thermal performance in 10^{-4} torr (vacuum) and 20-mbar atmospheres. During the simulated launch phase depressurization at ambient temperature the foam insulation system failed explosively. Subsequent analyses were unable to determine the exact cause of the failure. The fiberglass insulation system passed all tests with no noticeable degradation in performance.

The thermal conductivity of the fiberglass sample was also evaluated at several environmental conditions in a guarded hot-plate calorimeter. The results of these tests are compared with those from the thermal diffusivity tests and with data from the literature in Fig. 11.

Subsequent to the completion of this study, a JPL evaluation indicated that performance comparable to that of the fiberglass system could be achieved using two layers of metalized plastic films to create dead-air spaces. This system also outperformed the conventional multilayered superinsulation by taking advantage of the low thermal conductivity of the CO_2 gas at low Mars atmospheric pressure. A substantial weight savings would thus be effected. Further testings will be necessary to confirm the validity of the study.

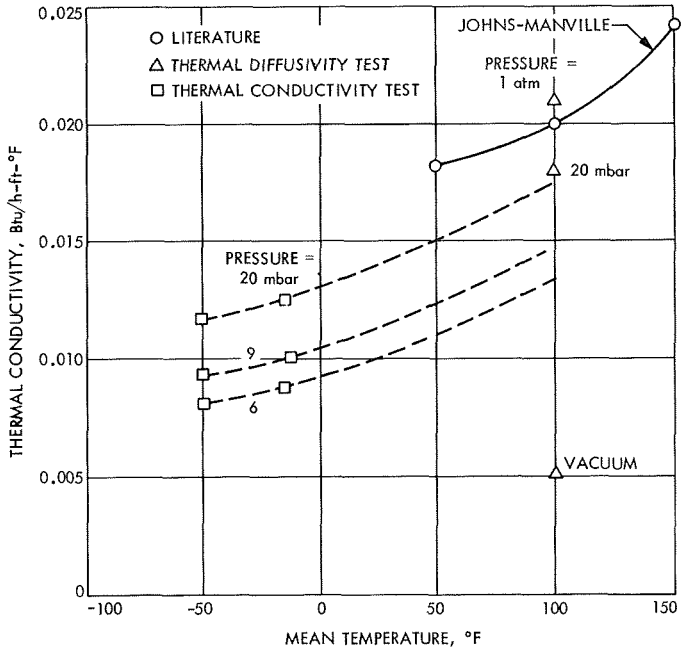

Fig. 11. Test data comparison for fiberglass thermal conductivity

Subject Index

Subject	Pages
Control and Guidance	
Mariner Mars 1971 scan calibration plan	12–14
logic initialization for *Mariner* Mars 1971 scan control electronics	14–15
thrust vector control for *Viking* orbiter three-engine propulsion system option	33–37
Electronic Components and Circuits	
logic initialization for *Mariner* Mars 1971 scan control electronics	14–15
Energy Storage	
post-encounter performance of *Mariner VI* battery	2–4
power subsystem support for *Mariner* Mars 1969 extended mission operations	4–8
pre-encounter anomalies in *Mariner VII* battery performance	4–8
Viking orbiter power subsystem	28–32
Ground Support, Spacecraft	
Mariner Mars 1971 system test complex cabling	20
***Mariner* Mars 1969 Project**	
project description and status	1–2
post-encounter performance of *Mariner VI* battery	2–4
power subsystem support for extended mission operations	4–8
pre-encounter anomalies in *Mariner VII* battery performance	4–8
***Mariner* Mars 1971 Project**	
project description and status	9–11
solar panel design, fabrication, and testing	11–12
scan calibration plan	12–14
logic initialization for scan control electronics	14–15
rocket engine thermal tests	15–20
thermal blanket tests	15–20
system test complex cabling	20
Materials, Nonmetallic	
insulation materials for a Mars lander	37–38
Mechanics	
thrust vector control for *Viking* orbiter three-engine propulsion system option	33–37
Particle Physics and Nuclear Reactions	
radiation hazards to orbiter produced by *Viking* lander radioisotope thermoelectric generators	32–33
Planetary Atmospheres	
Viking lander atmospheric analysis experiment	22–28
Planetary Surfaces	
Viking lander soil analysis experiment	22–28
Power Sources	
power subsystem support for *Mariner* Mars 1969 extended mission operations	4–8
Mariner Mars 1971 solar panels	11–12
Viking orbiter power subsystem	28–32
radiation hazards to orbiter produced by *Viking* lander radioisotope thermoelectric generator	32–33
Propulsion, Liquid	
Mariner Mars 1971 rocket engine thermal tests	15–20
thrust vector control for *Viking* orbiter three-engine propulsion system option	33–37
Scientific Instruments	
gas chromatograph/mass spectrometer for *Viking* lander system	22–28
Telemetry and Command	
telemetry channel assignments for *Viking* orbiter power subsystem	28–32
Temperature Control	
Mariner Mars 1971 rocket engine thermal tests	15–20
Mariner Mars 1971 thermal blanket tests	15–20
insulation materials for a Mars lander	37–38
Test Facilities and Equipment	
Mariner Mars 1971 system test complex cabling	20
***Viking* Project**	
project description and status	21
gas chromatograph/mass spectrometer for lander system	22–28
orbiter power subsystem	28–32
radiation hazards to orbiter produced by lander radioisotope thermoelectric generators	32–33
thrust vector control for orbiter three-engine propulsion system option	33–37
insulation materials for a Mars lander	37–38

NASA — JPL — Coml., L.A., Calif.